INSTITUTE OF PHYSICS PUBLISHING REPORTS ON PROGRESS IN PHYSICS

Rep. Prog. Phys. **66** (2003) 1145–1206 PII: S0034-4885(03)31552-0

Energy spectrum and mass composition of high-energy cosmic rays

Andreas Haungs, Heinigerd Rebel[1] **and Markus Roth**

Institut für Kernphysik, Forschungszentrum Karlsruhe, POB 3640, D-76021 Karlsruhe, Germany

E-mail: rebel@ik.fzk.de

Received 4 February 2003
Published 18 June 2003
Online at stacks.iop.org/RoPP/66/1145

Abstract

Primary cosmic rays above energies of about 100 TeV are investigated by observations of extensive air showers (EAS) using large area ground based detector installations for registering various components of the EAS cascade development. By such indirect studies of the primary cosmic rays a steepening of the power-law spectrum at around 3–5 PeV, known as the knee, has been identified. At higher energies around 5 EeV there appears a further change of the spectral index towards a flattening of the spectrum, called the ankle. The energy region above ca 50 EeV, where a cut-off of the cosmic ray spectrum (Greisen–Zatsepin–Kuz'min (GZK) cut-off) is theoretically predicted, is of particular current interest and provides an astrophysical enigma, since obviously trans-GZK events have been observed. Any explanation of these features of the cosmic ray spectrum needs sufficiently detailed knowledge of the shape of the spectrum and of the variation of the mass composition of cosmic rays. In this paper different experimental approaches deducing mass and energy sensitive information from the EAS experiments and their results are discussed. The experiments involve measurements of secondary particle distributions at various observation levels and of muons by deep underground detectors, as well as measurements of air Cherenkov light and, in particular at higher energies, of air fluorescence light emitted during the EAS development. Recently, methods for analysing multi-dimensional EAS parameter distributions have been favoured. They take into account correlations of different EAS parameters and, in particular by non-parametric techniques, also the influence of the intrinsic fluctuation of the air shower development. This paper illustrates the application of such methods in a coherent view of recent results. The advanced analysing methods are corroborated by hybrid experimental set-ups registering a larger set of different EAS observables simultaneously in an event-by-event mode. In addition such approaches provide the possibility to test the consistency of the hadronic interaction models and Monte Carlo procedures used as reference for the analyses. The physical and astrophysical implications of the current findings in various energy regions are briefly discussed and prospects of future experiments are presented.

[1] Author to whom correspondence should be addressed.

0034-4885/03/071145+62$90.00

Contents

1. Introduction

The all-particle energy spectrum of primary cosmic rays extends from 1 GeV to above 10^{20} eV (or 100 EeV), the highest energies of known individual particles in the universe. In spite of many efforts, we have still only a rudimentary understanding of, where these particles are coming from, how they are accelerated to such extremely high energies, how they propagate through interstellar space, and in addition how they interact with matter.

The flux of primary cosmic rays falls from 1 particle per m^2 s to 1 particle per km^2 century at highest energies. The energy spectrum appears rather featureless and follows an overall power-law $I(E) \propto E^{\gamma}$, indicating the non-thermal character, but with some characteristically distinct changes of the spectral index γ, first from -2.7 to ≈ -3.1 around 10^{15} eV, called the knee (figure 1). This feature was discovered 40 years ago by German Kulikov and George Khristiansen of the Moscow State University [1] within studies of the intensity spectrum of the content of charged particles of extensive air showers (EAS), which roughly reflects the primary energy. The key questions of the origin of the knee are still not convincingly solved.

A great deal of interest and current efforts concern the shape of the spectrum in the EeV region, above 10^{18} eV, where the spectrum seems to flatten (ankle) again, and especially around 6×10^{19} eV, with the theoretically predicted Greisen–Zatsepin–Kuz'min (GZK) cut-off [5, 6], due to the photo-interaction of protons with the 2.7 K primordial background radiation. In particular, the AGASA experiment in Akeno (Japan) [7] and former (preliminary) observations with the Fly's Eye installation (Utah, USA) [8, 9] seem to show that this limit of the cosmic ray spectrum does probably not exist. This fact is an issue of extreme astrophysical and cosmological relevance.

One of the difficulties of the studies is that cosmic rays are overwhelmingly charged particles, and the galactic and intergalactic magnetic fields are sufficiently strong to scramble their paths. Perhaps, except for those with highest energies, cosmic rays have lost all their memory about the location of the emission sources when they eventually arrive at the Earth's atmosphere. Hence the only observable quantities, which may give us some information are the energy distribution and the elemental composition of primary cosmic rays. At highest energies above 10^{18} eV the search for possible deviations from isotropic incidence (anisotropies) becomes important, since there is a chance of locating emission sources.

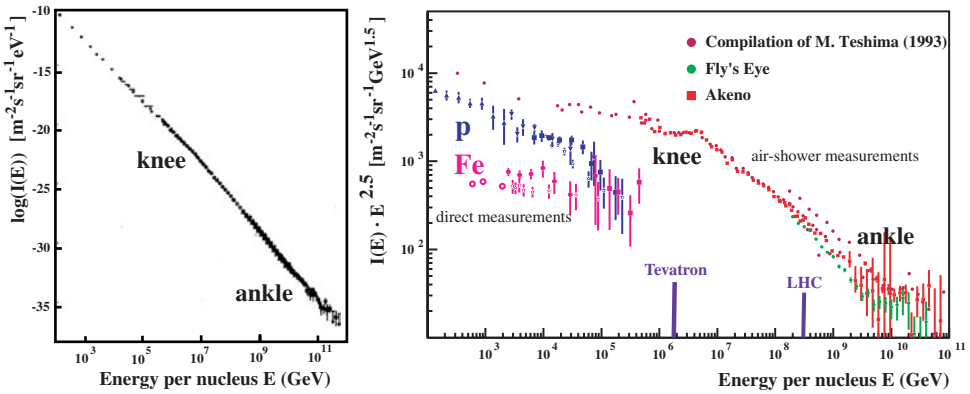

Figure 1. Primary energy spectrum of cosmic rays (in the right part the flux $I(E)$ is multiplied by $E^{2.5}$) (figures after [2, 3], compilation on the right-hand side from [4]). The equivalent beam energies of the Tevatron and Large Hadron Collider are indicated.

Below 10^{14} eV the flux of particles is sufficiently large that individual nuclei can be studied by flying detectors in balloons and satellites. From such direct experiments we know that the majority of particles are nuclei of common elements from hydrogen to iron. Around 1 GeV the quantities are similar to those found in ordinary material of the solar system. Striking exceptions are the abundance of elements like Li, Be, and B—overabundant since they originate from spallation of heavier nuclei in the interstellar medium.

At higher energies, where this report is focused, we rely on observations of EAS providing indirect information, in the sense that we do not directly determine energy and mass of the primary cosmic particles. The information searched for is inferred from secondary effects, from the lateral and longitudinal development of the particle cascades initiated by the primary cosmic particles in the atmosphere. These techniques require a good knowledge of the shower development in the atmosphere and of the interaction mechanisms of high-energy particles with air molecules. Extensive Monte Carlo (MC) simulation procedures are used as reference patterns. For the high-energy hadronic interactions more or less bold extrapolations from lower energies, formulated as theoretical models and parameterizations, are at disposal. For example, at the knee energies accelerator data are not yet available (though the Tevatron collider is close to these energies) either for relevant target–projectile combinations or for the kinematic region of secondaries scattered in the extreme forward direction. This situation leads to an uncertainty of unknown order, in some sense only to be guessed by using the same reconstruction procedures but different hadronic interaction models. Though, in the last few years, the improved understanding of the high-energy hadronic interaction has reduced larger disagreements in predictions of air-shower observables [10], it remains unclear if there are common systematic uncertainties in the interaction models by unknown features and interaction paths, not yet taken into account. Hence, results of air-shower experiments may be considered from different aspects. In addition to the astrophysical information about the shape of the primary energy spectrum and the elemental composition in absolute scales, the study of hadronic interaction features and of the EAS development are issues of equivalent importance, but strongly entangled with the other aspects. In fact the validity of the hadronic interaction models used as generators of MC simulations has become an important subject in the context of EAS analyses. These aspects have been emphasized in the last few years by the possibilities of multi-detector installations (i.e. hybrid experiments, e.g. [11, 12]) which enable cross-checks and studies of correlated EAS features characteristic of the properties and interaction of the primaries. Nevertheless co-operation between present and future accelerator experiments and the cosmic ray investigations is aspired to, and would help to constrain the basic interaction features.

This paper reports about the current experimental activities of studying high- and ultra-high-energy cosmic rays (in particular around the knee, the ankle and above). Together with the specific motivations of the experiments the presentation emphasizes the description of the methodical features of EAS observations and of the various analysing methods. It will be seen that many basic questions of the topic still remain open, and the review reports only about the present status in attacking the long-standing questions about energy spectrum and mass composition of high-energy cosmic rays.

2. Techniques and observables of EAS measurements

2.1. Extensive air showers

Above 10^{14} eV the techniques used to study cosmic rays exploit the phenomenon of EAS discovered in 1938 independently by Auger [13] and Kohlhörster [14] and communicated by timely overlapping publications.

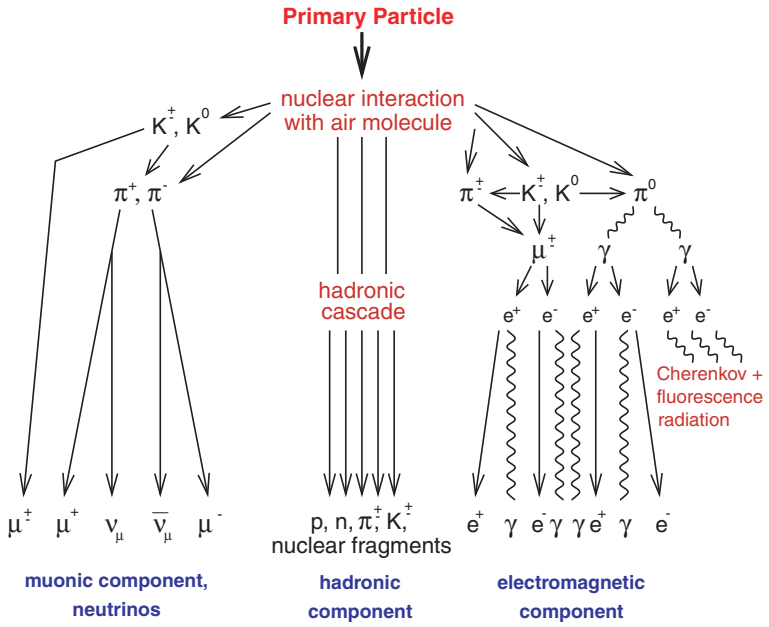

Figure 2. EAS progeny.

Most of the particles (figure 2) produced in hadronic collisions with air nuclei are pions and kaons, which can decay into muons and neutrinos before interacting, thus producing the most penetrating component of atmospheric showers: the muon component. The most intense component—electrons and photons—originates mainly from the fast decay of neutral pions into photons, which initiate electromagnetic showers, thus distributing the originally high energy of one primary particle over millions of charged (and neutral) secondary particles.

The longitudinal development of the electromagnetic component shows a growth, a maximum and a decay as the energy of the shower is dissipated. In contrast the muon cascade (called the penetrating component) grows and maximizes, but the decay is only slow as a consequence of the relative stability of the muon and small energy losses by ionization and pair production. The backbone of an air shower is the hadronic component of nucleons, pions and other particles, which feeds the electromagnetic and muonic components. It is often stated that the hadronic component is well concentrated around the shower axis. Nevertheless due to multiple scattering, neutrons in particular, are also distributed far off the centre.

The longitudinal EAS profile, i.e. the development of the number of charged particles (shower size) with the cumulated atmospheric depth X (the atmospheric thickness already crossed) can be adequately parameterized by the Gaisser–Hillas function [16], for the electron size, e.g.

$$N_e(X) = N_e^{\max} \cdot \left(\frac{X - X_0}{X_{\max} - X_0}\right)^{(X_{\max}-X_0)/\lambda} \cdot \exp\left(\frac{X_{\max} - X}{\lambda}\right) \tag{1}$$

with X the depth at observation, X_0 the depth of the first interaction, and $X_{\max}$ the depth of the shower maximum. The attenuation parameter λ is about 70 g cm^{-2}. The difference $(X_{\max} - X_0)$ depends on the energy E_0 and the nature of the primary and the difference $(X - X_{\max})$ is an indicator of the stage of development and increases approximately logarithmically with the energy. According to the superposition model which considers a heavy primary A as a swarm

of A nucleons of correspondingly reduced energy, the position of $X_{\max}$ depends on E_0/A so that the shift of $X_{\max}$ for an EAS induced by a nucleus is proportional to $\ln A$ and leads to a shift $(X^{\mathrm{p}}_{\max} - X^{\mathrm{Fe}}_{\max}) \approx 100\,\mathrm{g\,cm^{-2}}$. This is an essential feature for the mass discrimination. Thus MC simulations show clear differences in the average longitudinal development of EAS induced by different primaries (figure 3). The shower development of a heavy ion induced shower starts earlier, and reaches the maximum earlier than is the case for proton induced showers of the same energy. Gamma ray induced showers would show much less fluctuation and are poor in muons due to the small cross-sections of meson production by photons and electromagnetic muon pair creation.

The charged particles, particularly the electromagnetic component, are accompanied by an additional EAS phenomenon, the production of atmospheric Cherenkov light which carries information about the longitudinal shower development, especially about the height $X_{\max}$ of the shower maximum. At higher energies the shower can be efficiently observed by the fluorescence light of N_2 molecules, induced by the charged particles in air. Air fluorescence observations are able to reconstruct the longitudinal shower profile. However, Cherenkov and fluorescence light observations require absence of light background. In general, they need clear moonless nights and have consequently a lower duty cycle for the observations compared to the technique of charged particle detection.

There is another phenomenon accompanying the EAS development: radio emission experimentally discovered by Jelly *et al* [17] in 1965. The effect was already predicted in 1962 by Askaryan [18] as arising from the annihilation of positrons which would lead to a negative

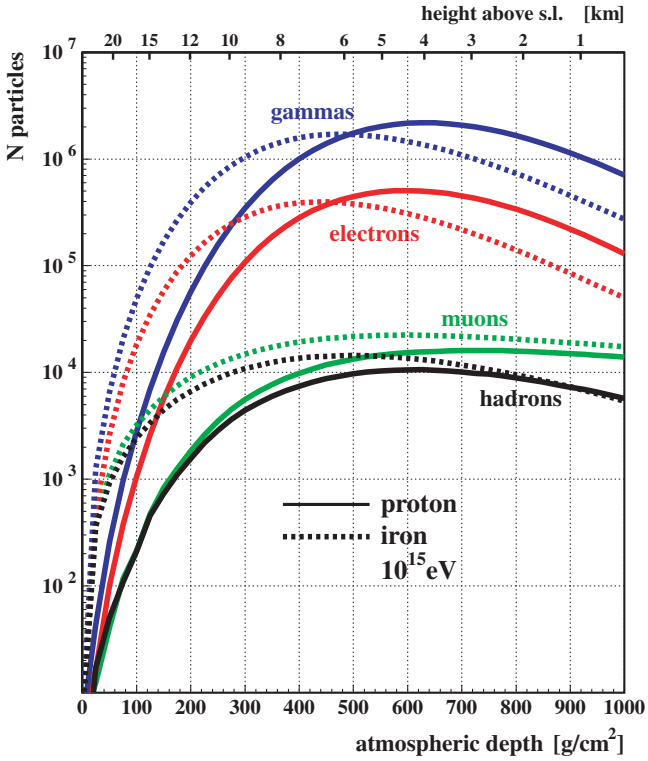

Figure 3. Longitudinal EAS development of the average total intensities (sizes) of different particle components of EAS of vertical incidence (from MC simulations by CORSIKA [15]).

charge excess in the EAS and in this way to Cherenkov radiation when rushing through the atmosphere. The dependence on the geomagnetic field detected by later experiments, however, suggests a different origin of radio emission in air showers: 'synchrotron' radiation produced by the electron and positron paths in the geomagnetic field. Since the radio flux is expected to grow quadratically with the number of particles, this particular EAS component induced recently some new interest as an alternative method of EAS detection due to the increased sensitivity provided by modern antenna and receiver technology.

In general with ground-based experiments of large detector arrays, we are hardly in the position to register the longitudinal development. We observe only the developed status of the air-shower cascade at the observation level of the detectors. From the observables registered there, that means from the total number (size) of the various particle components, the lateral (figure 4) and accessible energy distributions, and eventually arrival time profiles of the shower disk, we have to deduce the properties of the primary particle.

The particle numbers and the width of the lateral distributions of the three components are very different (see figure 4). The muons, for example, extend to several hundred metres (and even a few kilometres for the highest primary energies) as many of them are produced very high in the atmosphere. Therefore, even a small transverse momentum imparted to them in the production process can lead to large lateral distances from the shower axis at the observation level. In standard EAS experiments the lateral distributions of the particles are sampled by more or less regular arrangements of a large number of detectors which cover only a small fraction of the total area. This sampling allows us to extrapolate to total particle numbers, but is an additional source of instrumental fluctuations which add to the large spread resulting from the inherent statistical fluctuations due to the stochastic shower development in the atmosphere.

Figure 5 schematically sketches different experimental techniques for the observation of experimentally defined parameters, which adequately characterize the EAS.

2.2. *EAS experimental techniques*

Table 1 compiles various EAS experiments which have contributed results relevant for this discussion or are going to contribute to EAS studies by registering different EAS observables. Many of them, in particular those which have been dedicated to studies of the knee region

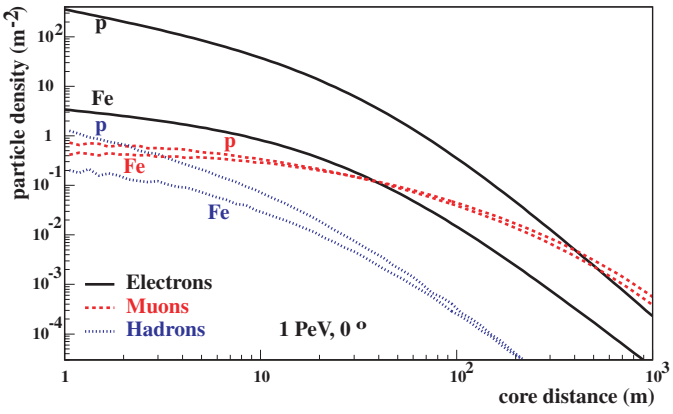

Figure 4. Lateral distributions of the particle densities of different charged particle EAS components (by CORSIKA [15] MC simulations with primary energy of 10^{15} eV and vertical incidence of protons).

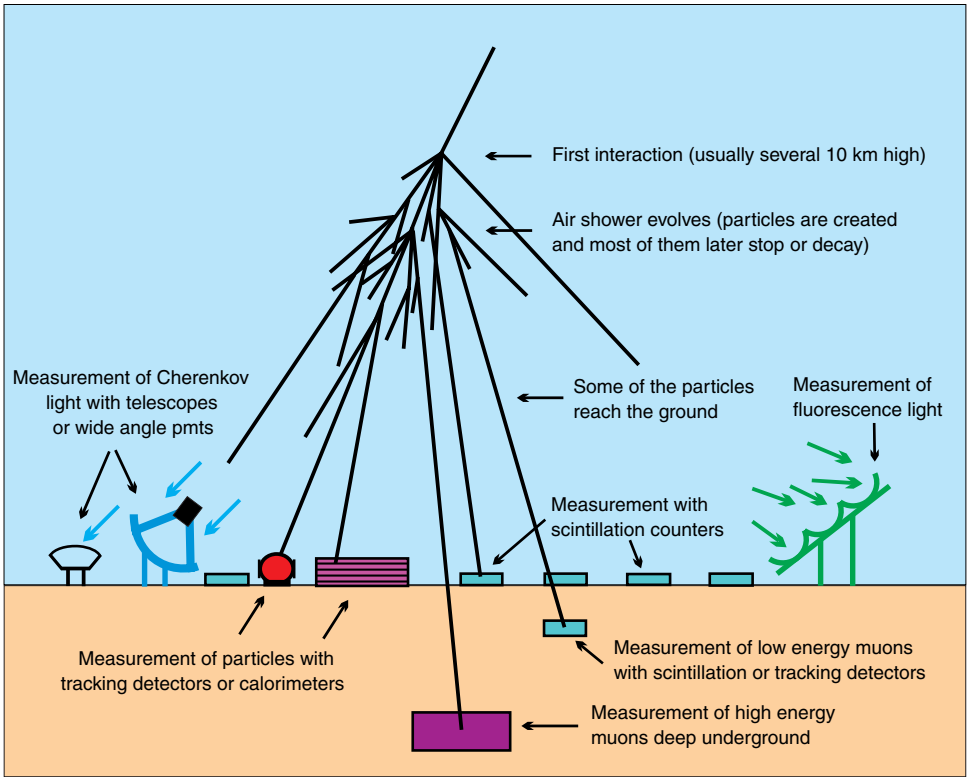

Figure 5. Sketch of EAS measurements (after [19]).

or which are able to register only a rather restricted number of observables, are no longer operated (nlo). Motivated by advanced analysis techniques modern installations are designed to measure simultaneously as many parameters of different EAS components as possible.

Just as one example the photo (figure 6) shows the KASCADE detector arrangement [11], installed in Forschungszentrum Karlsruhe. The special feature of this multi-detector experiment is the so-called central detector in the centre of the array, which consists basically of a 300 m^2 hadron calorimeter measuring various parameters of the hadronic component. The KASCADE experiment combines the observation of the electromagnetic and muon components with measurements of the hadronic component. Other hybrid installations measure simultaneously with the charged particles, the Cherenkov light or, at higher energies, the air fluorescence light.

In the following we discuss some details of various EAS features which lead to observable quantities, to be analysed in terms of the properties of the primary inducing the EAS in the atmosphere.

2.2.1. Charged particle component. The measurement of the charged particle component provides the basic information in all EAS experiments. Due to the dominance of electrons and positrons (and gamma rays) of the secondary particles of an air-shower at and after the maximum of the development, the EAS is first of all characterized by the total number of charged particles, called shower size N_{ch}. Many early investigations do not sharply differentiate between the total electron number and that of charged particles, $N_e \approx N_{ch}$. The observation

Table 1. EAS experiments.

Experiment	Location	Detector	Observables	References
CASA (nlo)	Dugway, Utah, US	Scint. array	N_e	[20]
MIA (nlo)	870 g cm^{-2}	μ-underground	N_μ	[21]
BLANCA (nlo)	W 112.8 N 40.2	Č-light	X_{max}	[22]
DICE (nlo)		2 imag. Č-telesc.	X_{max}	[23]
HEGRA (nlo)	La Palma (Canary Isl.)	Scint. array	N_e	[24]
AIROBICC	790 g cm^{-2}	Č-light	X_{max}	[25]
	W 17.9 N 28.8	CRT	Part. tracking	[26]
MSU (nlo)	Moscow, Russia	Scint. array	N_e	[27]
	1000 g cm^{-2}	μ-underground	μ	[28]
EAS-TOP (nlo)	Gran Sasso, Italy	Scint. array	N_e	[29]
	810 g cm^{-2}	h-μ-calorimeter	N_μ, h	
MACRO (nlo)	Undergr. 3100 m w.e.	μ-Tracking	Multi-μ	[30]
	E 13.6 N 42.4	($E_\mu > 13$ TeV)		
AKENO (nlo)	Akeno, Japan	Scint. array	N_e	[31]
	920 g cm^{-2}	μ-counter	N_μ	[32]
	E 138.5 N 35.8	Č-counter	X_{max}	
KASCADE	Karlsruhe, Germany	Scint. array	N_e, N_μ	[11]
	1020 g cm^{-2}	LST-tunnel	μ-Tracking	[33]
	E 8.4 N 49.0	Calorimeter	N_h, E_h	[34]
		MWPC, LST,	N_μ, ρ_μ	[35]
		Scint.	μ-Arrival times	
KASCADE-Grande		Scint. array	N_{ch}	[36]
MAKET-ANI	Mt Aragats, Armenia	Scint. array	N_e	[37]
GAMMA	700 g cm^{-2}	Scint. array	N_e	[38]
	E 45.2 N 41.2			
TIBET ASγ	Yanbajing, China	Scint. array	N_e	[39]
ARGO	606 g cm^{-2}	RPC-carpet	N_{ch}	[40]
	E 90.5 N 30.1		μ-Multiplicity	
Haverah Park	Yorkshire, UK	Water Č-array	N_e, rise times	[41]
(nlo)	1020 g cm^{-2}			
Grex/	W 1.6 N 56.0	RPC stack	Arrival times	[42]
cover-plastex				
AGASA	Akeno, Japan	Scint. array	N_{ch}	[7]
	920 g cm^{-2}			
	E 138.5 N 35.8			
Yakutsk	Russia	Scint. array	N_e,N_μ	[43]
	1020 g cm^{-2}	Č-light	X_{max}	
	E 129.4 N 61.7	μ-underground		
Fly's Eye	Dugway, Utah, US	FD-telescope	Fluor. light	[44]
(nlo)	870 g cm^{-2}			
	W 112.8 N 40.2			
HiRes Fly's Eye	Dugway, Utah, US	FD-telescopes	Fluor. light	[45]
	870 g cm^{-2}			
	W 112.8 N 40.2			
AUGER	Argentina	Water Č-array	N_e, N_μ	[12]
	875 g cm^{-2}	FD-telescopes	Fluor. light	
	W 69.3 S 35.5			

Table 1. EAS experiments.

Experiment	Location	Detector	Observables	References
NORIKURA (nlo)	Japan, 740 g cm^{-2} E 137.3 N 36.1	Scint. array	N_e	[46]
GRAPES III	Ooty, India 600 g cm^{-2}	Scint. array Prop. counters	N_e N_μ	[47]
SPASE VULCAN (nlo)	Southpole 650 g cm^{-2}	Scint. array Č-light	N_e X_{max}	[48]
Tien-Shan	Kyrgyzstan 690 g cm^{-2}	Scint. array Č-light	N_e X_{max}	[49]
L3+C (nlo)	CERN, Switzerland 1000 g cm^{-2} E 6.01 N 46.15	Scint. array μ-tracking ($E_\mu > 15$ GeV)	N_e μ-Multip., E_μ	[50]
Tunka 13	Russia, 950 g cm^{-2} E 103 N 51.5	Č-light	X_{max}	[51]
BAKSAN BUST	Russia, 833 g cm^{-2} E 42.7 N 43.4	Scint. array Undergr. array	N_e Muons	[52] [53]
Mt Chacaltaya BASJE	Bolivia, 540 g cm^{-2} W 68.2 S 16.4	Emulsion Ch. Scint. array	$h + \gamma$ N_e	[54]
PAMIR	Tadjikistan 600 g cm^{-2}	Emulsion Ch.	TeV $h + e/\gamma$	[55]
Mt Kanbala	Japan 520 g cm^{-2}	Emulsion Ch.	TeV $h + e/\gamma$	[56]
Mt Fuji	Japan 650 g cm^{-2}	Emulsion Ch.	TeV $h + e/\gamma$	[57]

Figure 6. Photo of the KASCADE detector array.

of the charged particle component also enables a determination of the angle-of-incidence and of the axis of the shower.

In all experiments the measurement and experimental reconstruction of the shower size is performed by use of basically similar standard procedures: an array of detectors distributed

over an area of several thousands of square-metres samples the particle and/or Cherenkov light densities. The lateral density distributions and integral quantities of them are analysed (adopting some experiences gained by MC simulations) to infer the primary energy of the incident particles, either for single events or more often for the average of the measured distributions. It should be noted that the conversion of observed pulse heights in the detectors to the particle numbers and the conversion to the primary energy are not really straightforward since the number of registered particles is only a small fraction of the total number.

For the lateral density distribution function (LDF) of charged particles various functional forms are in use. The shapes of the lateral distributions of different charged particles in showers are described mainly by functions which led to the first type Euler integrals (plus some modifications) or by exponential functions. Generally they are of phenomenological nature, specifically adapted to the particular detector array under consideration. Since the arrays differ in detection thresholds, detector response and observation level, in general they are not comparable with each other. In order to give an impression about the variety of forms in use, the most popular LDFs are briefly characterized:

(a) The Nishimura–Kamata–Greisen (NKG) approximation [58, 59]

$$\rho_{\mathrm{ch}}(r) = \frac{N_{\mathrm{ch}}}{2\pi r_0^2} \cdot C \cdot \left(\frac{r}{r_0}\right)^{s-2} \cdot \left(1 + \frac{r}{r_0}\right)^{s-4.5} \tag{2}$$

with N_{ch} the total number of charged particles, and s the so-called (lateral) age parameter which describes the shape of the particle distribution and is theoretically related to the status of the longitudinal development. r_0 describes the Molière radius, defined within the multiple scattering theory, $\approx$79 m at sea level, i.e. atmospheric thickness of 1033 g cm^{-2}. It is the distance within which 90% of the total EAS energy is contained, $C = \Gamma(4.5 - s)/\Gamma(s)\Gamma(4.5 - 2s)$ denotes a constant with the gamma function Γ.

This approximation is widely used in cosmic ray experiments for describing the electron and charged particle distributions. The NKG function is based on a theoretical description of purely electromagnetic showers. Though it is often adopted to describe also hadronic showers, that is only approximately correct. Therefore more phenomenological LDFs have been alternatively introduced.

(b) The Greisen approximation [60, 61]

$$\rho_{\mathrm{ch}}(r) = \frac{N_{\mathrm{ch}}}{2\pi r_0^2} \cdot C_1 \cdot \left(\frac{r}{r_0}\right)^{s-2} \cdot \left(1 + \frac{r}{r_0}\right)^{s-4.5} \cdot \left(1 + C_2 \left(\frac{r}{r_0}\right)^{d}\right), \tag{3}$$

where $C_1 = [B(s, 4.5 - 2s) + C_2 B(s + d, 4.5 - d - 2s)]^{-1}$, and in Greisen's paper $C_2 = 1/11.4$ and $d = 1$, whereas B is the Euler-function.

(c) A phenomenologically improved modification of the description of large showers registered with the Akeno array is [31]

$$\rho_{\mathrm{ch}}(r) = \frac{N_{\mathrm{ch}}}{2\pi r_0^2} \cdot C_3 \cdot \left(\frac{r}{r_0}\right)^{s-2} \cdot \left(1 + \frac{r}{r_0}\right)^{s-4.5} \cdot \left(1 + \beta \frac{r}{r_0}\right)^{\nu} \tag{4}$$

for which an analytical integration from zero to infinity cannot be given.

(d) The Haverah Park experiment represents successfully the lateral signal density $S(r)$ induced by the charged particles in the water-Cherenkov detectors by

$$\begin{aligned} S(r) &= k\, r^{-(\eta + r/r_0)} \qquad \text{for } r < 800\,\mathrm{m} \\ S(r) &= \left(\tfrac{1}{800}\right)^{\beta} kr^{-(\eta + r/r_0) + \beta} \qquad \text{for } r > 800\,\mathrm{m} \end{aligned} \tag{5}$$

with the shape parameter η varying with zenith angle and $r_0 = 4000$ m, independent of zenith angle [62]. Actually the η-parameter has been shown to carry some mass sensitivity of EAS above 3×10^{17} eV [63].

(e) Some other experiments (e.g. [64]) used the following approximation:

$$\rho_{\mathrm{ch}}(r) = \frac{1.75 \times 10^{-3} N_{\mathrm{ch}}}{r} \exp\left(-\frac{r}{80\,\mathrm{m}}\right) \qquad \text{for } r = 3\text{–}140\,\mathrm{m}$$
$$\rho_{\mathrm{ch}}(r) = 2.25 \cdot N_{\mathrm{ch}} r^{-2.8} \qquad \text{for } r = 140\text{–}1000\,\mathrm{m}. \tag{6}$$

Greisen modified the NKG formula (equation (2)) in 1960 [60] in order to take into account the different and more extended lateral distribution of EAS muons at large distances from the axis. There are also some attempts to modify the NKG formula (equation (2)) in order to obtain a better description of the average lateral distribution of charged particles of showers [65] observed at high-mountain altitudes (at Mt Chacaltaya 5200 m a.s.l.):

$$\rho_{\mathrm{ch}}(r) = \frac{1.03 \cdot N_{\mathrm{ch}} \cdot C_1}{2\pi r_0^2} \cdot \left(\frac{r}{r_0}\right)^{s-2} \cdot \left(1 + \frac{r}{r_0}\right)^{s-4.5} \times \left(1 + C_2 \left(\frac{r}{r_0}\right)^2\right) \cdot \left(1 - 0.2 \cdot \exp \frac{-(\ln (r/r_0) + 0.3)^2}{0.5}\right), \tag{7}$$

where C_1 and C_2 are constants with values obtained by fitting to the experimental data.

The total charged particle number, i.e. the integrated LDF, is related to the primary energy, but the relation depends on the type of the primary. A compilation of recent shower size spectra in the knee region of different experiments is given in figure 7. The knee structure is obvious in all spectra, but the figure also illustrates the difficulty and discrepancies of comparing various experiments. Not only the knee positions, but also the shapes of the spectra differ according to different observation levels, zenith distances, and different particle detection thresholds and due to taking into account the detector response in an insufficient way. Recent analyses examine possible fine structures of the spectra of the knee region by compiling size spectra of a large number of experiments. While Erlykin and Wolfendale [71] claim to identify some indications for modulations of the shape, the results of Schatz [72] are in agreement with a smooth knee transition without any conspicuous substructures.

2.2.2. Muon component. The less copious but penetrating EAS muons are mostly measured by shielded detectors (scintillators, Geiger–Müller counters, limited streamer tubes, proportional counters) or unshielded water Cherenkov detectors, whereby the punch-through of hard gamma rays or electrons has to be minimized. Alternatively some tracking procedures are used to identify the muons.

Observables are the total muon number, the lateral distribution of the muons, the muon arrival time, and/or the muon track angle relative to the shower axis. In a basically similar way as for the charged particle component the lateral muon density distribution is sampled and the total muon number (muon content or muon size) is determined.

The shape of the function of the lateral distribution of muon density in the showers for different threshold energies of the muons E_{th} (GeV) was given by Greisen 1960 [60]:

$$\rho_\mu(r) = \frac{14.4 \cdot r^{-0.75}}{(1 + r/320\,\mathrm{m})^{2.5}} \cdot \left(\frac{N_\mu}{10^6}\right)^{0.75} \cdot \frac{51\,\mathrm{GeV}}{E_{\mathrm{th}} + 50\,\mathrm{GeV}} \left(\frac{3}{E_{\mathrm{th}} + 2\,\mathrm{GeV}}\right)^{(0.14 \cdot r^{0.37})}. \tag{8}$$

This form has been simplified as approximation of the lateral distribution of muons in different experiments [73, 74]:

$$\rho_\mu(r) \propto r^{-\alpha} \exp\left(-\frac{r}{r_0}\right). \tag{9}$$

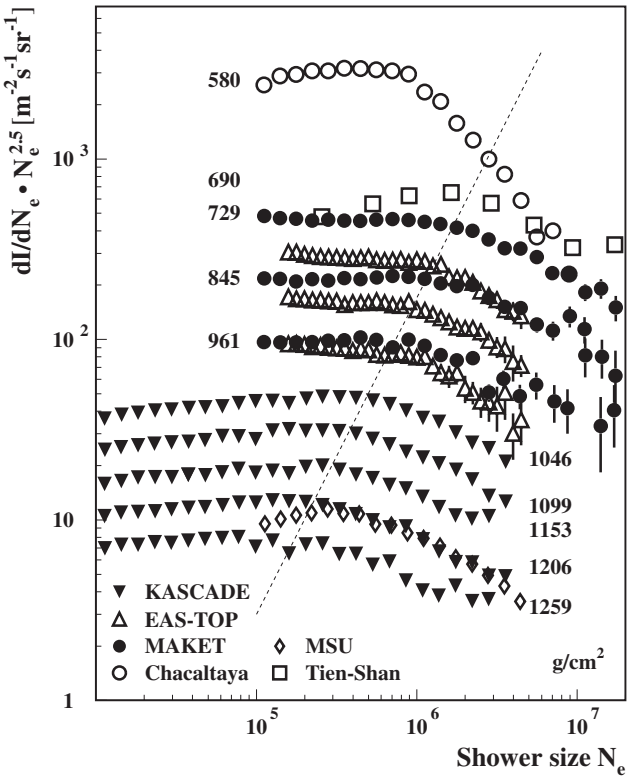

Figure 7. Shower size spectra observed in various experiments located at different altitudes and with different angles-of-incidence (indicated by the atmospheric grammage). The line is guiding the eyes to the knee positions in the spectra (KASCADE [66], EAS-TOP [67], MAKET [68], Chacaltaya [69], MSU [28], Tien-Shan [70]).

More or less phenomenologically derived factors are added depending on the experimental set-up (e.g. observation level, muon detection threshold energy and range of investigated core distance). For example, at Tien-Shan [75] data are fitted by

$$\rho_\mu(r) = 5.95 \times 10^{-4} r^{-0.7} \exp\left(-\frac{r}{80\,\mathrm{m}}\right). \tag{10}$$

The philosophy of the KASCADE experiment is to minimize the bias by the functional form of the muon LDF extrapolated to unobserved large distances from the shower axis. Therefore as useful quantity representing the EAS muon content the truncated muon number

$$N_\mu^{\mathrm{tr}} = 2\pi \int_{40\,\mathrm{m}}^{200\,\mathrm{m}} \rho_\mu(r) r \,\mathrm{d}r \tag{11}$$

has been introduced. It turns out that N_μ^{tr} can be used as an approximate mass independent energy estimator in case of the KASCADE experiment. KASCADE showed that the muon lateral distribution also can be parameterized by the NKG function (equation (2), with a modified value of r_0) in the restricted range of observations up to 200 m distance from the shower axis [76]. The resulting muon size spectra for different zenith angle ranges show clearly a knee structure (figure 8). In 1970 the Tien-Shan experiment was the first experiment which reported experimental evidence for the knee in the muon size spectrum [75].

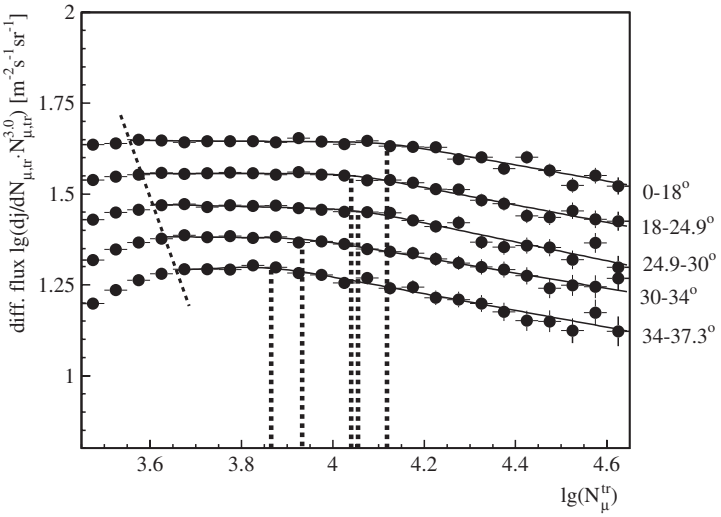

Figure 8. The truncated muon number size spectra of KASCADE [66] for different zenith angles. The knee and the full efficiency positions are indicated by dashed lines.

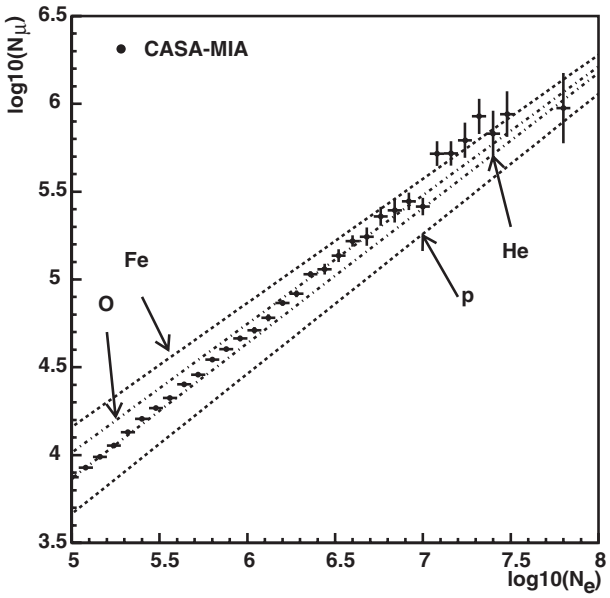

Figure 9. The muon to electron shower size correlation measured by the CASA-MIA experiment [78]. The data are compared to MC simulations of different primaries. The distribution is used for an estimate of the mass composition in the knee region.

In combination with the charged particle component the muon component is the most sensitive parameter to distinguish mass groups [77]. The correlation of the electron size to the muon size is used in many variants. Figure 9 shows the experimental variation of this correlation as observed by the CASA-MIA experiment [78]. The interpretation in terms of elemental composition needs the reference to MC simulations, shown for different kinds of primaries.

Tracking detectors allow not only an improved muon identification, but also allow us to reconstruct the angle of muon incidence relative to the shower axis and subsequently a determination of the muon production height, as far as multiple scattering effects do not obscure. Examples are the experiments with the HEGRA-CRT device [26] or the muon tracking detector of KASCADE [33]. Alternatively the relative arrival times of muons (i.e. the temporal structure of the muon disc) potentially maps the longitudinal EAS development and have been exploited, e.g. in the Haverah Park [79] experiments and at KASCADE [80]. Since the arrival time of the muons is expected to be earlier than for the electron–photon component, measurements of the rise time of the signal in the water Cherenkov tanks of Haverah Park were used for large EAS to discriminate electrons from muons [41]. For larger energies and core distances of ca 500 m the muons dominate the charged particle distribution. The signal density at 600 m is an established mass insensitive quantity for the energy estimate of experiments like AGASA [81].

2.2.3. Deep underground muons. EAS muons of very high-energy originate preferentially from the first interactions of the primary cosmic rays in the atmosphere. Thus they carry some information about the character of the primaries due to differences in the lateral distributions and in the muon energy spectrum between light and heavy nuclei induced EAS, and they are also sensitive to the mean transverse momentum transferred to the produced hadrons. Deep underground muon detectors with large energy thresholds in the TeV range measure single muons or muon bundles from ultra-high-energy cosmic rays. The difficulties in deducing the information arise from limitations introduced by the fluctuations in the muon multiplicity, by the multiple scattering and multi-muon production at the rock, by the finite dimensions of the detectors, and by the uncertainties in the energy of the associated EAS when the measurements are not correlated to surface detector arrays. A typical case is the analysis of measurements of the underground SOUDAN detector [82] comparing the multiplicity distribution for the muon energy threshold of 0.7 TeV with MC simulations for different composition models. Recently measurements of the MACRO detector have been combined with EAS-TOP observations (figure 10), or similarly the BUST device with the Andyrchy array at Baksan [52], as well as the former LEP detector L3 with an installation of a small scintillator array on the surface [50] in order to correlate different EAS observables. But only the EAS-TOP/MACRO experiment has so far published data of relevance for the primary cosmic ray energy spectrum and the mass composition. An interesting aspect of the LEP detectors is the possibility of muon energy determination and charge ratio measurements of atmospheric muons, which are of some importance for tests of MC models and for checks of calculations of the atmospheric neutrino flux.

2.2.4. Hadronic component. The hadronic EAS component has been prevailingly studied under the aspect of interactions of high-energy hadrons, which are observed at high-mountain altitudes with specially designed calorimeters (see section 2.2.5). Nevertheless the hadronic EAS component also provides useful information about the energy and nature of the primary, when observed in combination with other basic parameters, specifying the EAS. In addition to the number of hadrons (observed above a certain threshold) and the energy distribution of the hadrons, the spatial distribution of the hadrons in the shower core carries signatures of the primary particle in a similar way to that of the muons [85]. Actually there have been only a few attempts to operate adequate hadron calorimeters combined with standard EAS detector arrays. Some installations never got into operation (see, e.g. ANI-hadron calorimeter) or were only used for special studies [86]. At Mt Chacaltaya so-called burst counters have been used in combination with a scintillator array to infer information on mass composition [87]. Burst

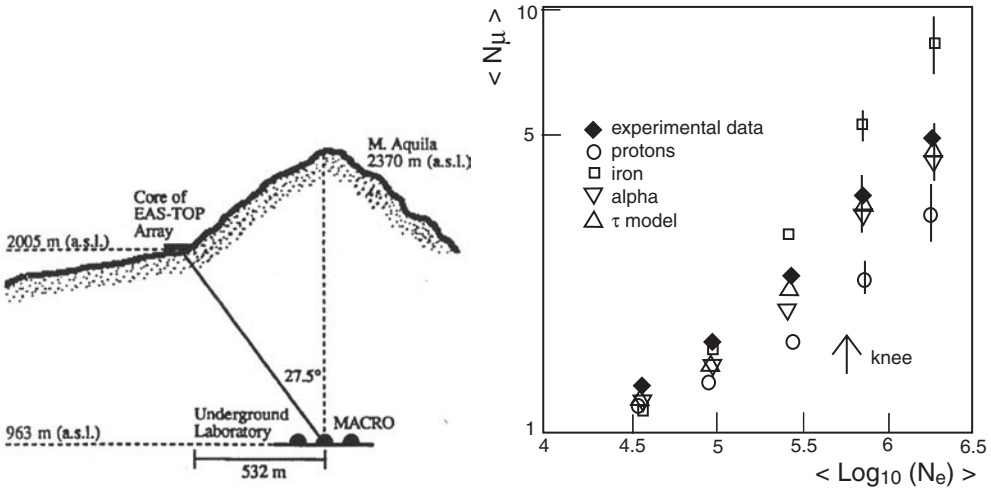

Figure 10. The dark matter detector MACRO combined with the EAS-TOP array for cosmic ray studies (from [83]). The muon multiplicity measured deep underground (>13 TeV) correlated with the shower size provides the mass sensitivity [84].

detectors are lead-emulsion plate sandwiches with a large lead shielding and time sensitive scintillation counters on top or below. The technique is only efficient at high altitudes due to the energy detection thresholds in the TeV range.

A large hadron calorimeter for detailed measurements of the spatial and energy distributions of hadrons in the air shower cores is in operation at the KASCADE experiment [34] at sea level. Detailed lateral distributions of hadron numbers and hadronic energies in air showers have been measured by using liquid ionization chambers as detectors. This iron-sampling calorimeter, covering an area of 300 m^2 [76], observes the energy transition curves of individual hadrons in the calorimeter for measuring the energy of the hadrons.

KASCADE has measured various observables of the hadronic component, in particular the number of hadrons (hadronic shower size) and their energy sum. In both observables the knee position has been identified in the PeV region [88]. For example, figure 11 shows the spectrum of the hadronic energy sum. The hadrons measured in shower cores at KASCADE are mainly used for consistency checks of the high-energy hadronic interaction models used in MC simulations of air-shower development [89–91].

2.2.5. EAS investigations at high-mountain altitudes with emulsion chambers. An emulsion chamber (EC) is sensitive to high-energy electrons, γ-rays and hadrons, incident on the chamber, and is able to determine the energies and positions of these particles with high precision. It is used to observe high-energy cosmic ray secondaries on high mountains, where the shower cascades can be observed in their early stages of development and with minimal fluctuations. A typical EC set-up (figure 12) consists at least of two lead-x-ray film sandwich chambers (Γ block and hadron block) of several m^2 area, separated by a layer of carbon and some spacer (see, e.g. [55]). The radiation length in lead is very short (6.37 g cm^{-2}) compared to the nuclear interaction length (ca 150 g cm^{-2}). Hence atmospheric photons and electrons initiate cascades very soon after entering the Γ block on top. Hadrons on the other hand interact deeper in the chamber. Interactions of hadrons above the detector would be expected to produce both hadrons and photons. A purely electromagnetic cascade in the atmosphere

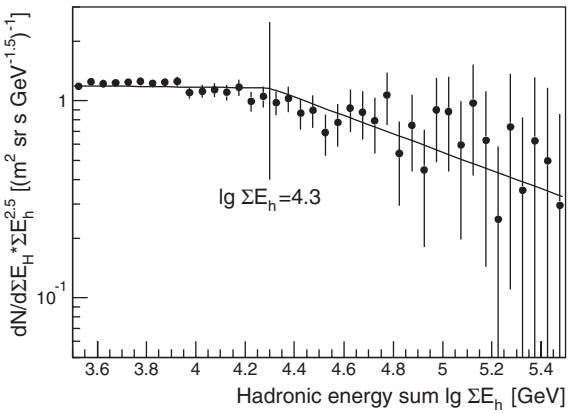

Figure 11. Flux spectrum of showers in the total hadronic energy measured by the KASCADE calorimeter. The observed knee is indicated by a vertical line (from [88]).

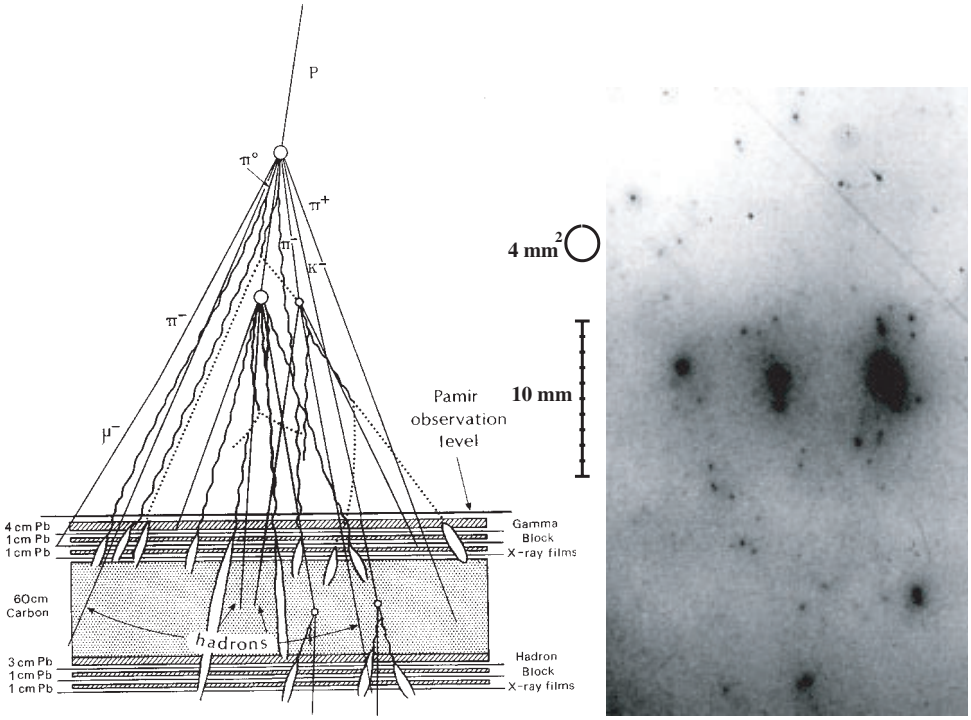

Figure 12. Schematic view of a typical emulsion experiment at high altitudes. Also shown is an example of developed x-ray film with some spots produced by TeV gamma rays (from [92]).

would manifest itself at the chamber as a group of cascades (so-called families) all starting near the top of the chamber. The observable in EC experiments is the so-called optical density of spots in micrometre sizes visible after development of the films with a typical exposure time of several months. The spot darkness is proportional to the γ-ray energy E_γ. The basic idea is to measure $\sum E_\gamma$, mostly resulting as cascade products from π^0 decays, and relate this sum to the primary energy.

The main objectives of mountain EC experiments are to study nuclear interactions, in particular in the extreme forward direction of the production of secondaries, and in energy regions exceeding those of man-made accelerators. For example, such experiments can be analysed in terms of the average inelasticity of hadronic collisions, i.e. the fraction of the collision energy which is transferred to the produced secondaries [93, 94].

An analysis of EC data (measured at Mts Fuji and Kanbala) in terms of the primary proton spectrum around the knee using modern analysing methods is given in [95]. At Mt Chacaltaya (5200 m a.s.l., Bolivia) a hybrid experiment has been carried out, where the EC technique has been combined with an air-shower array of 35 plastic scintillators, distributed over an circular area of 50 m, and with a hadron calorimeter located beneath the EC [96]. The observed distribution of the average number of registered hadrons is sensitive to the average mass of the primary mass composition and is evaluated, invoking the superposition hypothesis, where the average hadron number is known for proton induced showers of the same energy [97].

2.2.6. Cherenkov light observation. High-energy charged particles generate Cherenkov radiation which is strongly forward peaked with an opening angle of $\approx 1.2^{\circ}$ at the emission and can be measured on the ground with light-detector arrays. It is emitted by the shower cascade throughout the atmosphere and offers the possibility of measuring the total energy of the shower and of tracing the shower development. Due to the changing refractive index and the characteristic Cherenkov angle the lateral distribution has a particular structure, and the shape of the distribution around 100 m gets sensitive to the height of emission. The light from the early part, where the energies of the particles are still very high and the scattering angles small is concentrated in a characteristic ring near 100 m. The resulting lateral distribution is the superposition from all heights, and its shape depends on the shower development. If the shower maximum gets nearer to the ground, more light is produced near the shower core. That means the lateral distribution drops faster the closer the shower maximum is to the detector. There is a correlation between the distance to the shower maximum and the slope parameter of the lateral Cherenkov light distribution (see figure 13). This correlation proves to be independent of the type of the particle and the angle-of-incidence of the shower. The principle for mass discrimination with the help of the Cherenkov light is illustrated in figure 13.

The experiment HEGRA-AIROBICC [25] at La Palma, Spain (2200 m a.s.l.) is equipped with a scintillator array measuring the charged particle component (N_e, angle of shower incidence and core position) and with an array of open photomultipliers for the lateral

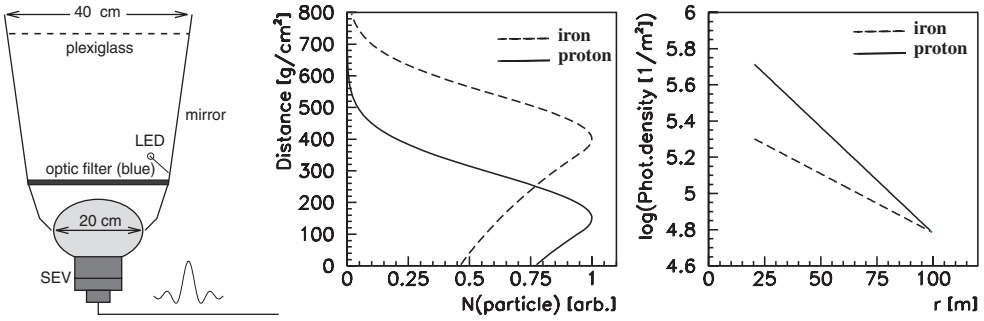

Figure 13. A typical detector for arrays measuring the EAS Cherenkov light (HEGRA-AIROBICC), and an illustration of the relation of the lateral Cherenkov light distribution to the longitudinal production of electromagnetic particles (after [98]).

distribution of the Cherenkov light registration, whereas the light is analysed in the interval 20–100 m from the shower core.

In observations of the Cherenkov light by the imaging technique, like in DICE [23], cosmic ray events within the field of view produce a focal plane image at a pixel camera built of photomultipliers, which is the intensity pattern of Cherenkov light coming from the air shower. When the direction of the air shower and the distance of the shower core from the telescopes are known, the amount of light can be reconstructed from each altitude of the shower. The amount of light is strongly correlated with the shower size, from which the height of maximum $X_{\max}$ can be determined. This procedure is essentially geometrical and is so far independent from MC simulations. However, the interpretation of the observed $X_{\max}$ distribution, which plays the role of an observable shower parameter, in terms of the elemental composition needs MC simulations with all their inherent model dependence.

The change of the position of the depth of the EAS maximum with energy per decade, the so-called elongation rate $D_{10} = \mathrm{d}X_{\max}/\mathrm{d}\log_{10} E$ is fairly constant. Within the superposition model approximation, i.e. assuming that for heavy primaries A the $X_{\max}$ dependence scales with E/A, the mean atmospheric depth of the maximum depends only on the energy per nucleon of the primary. This is confirmed by simulations, but affected by considerable fluctuations, which decrease with increasing mass number A and energy. Thus with the mean E/A deduced from the position of maximum $X_{\max}$ we gain information about the average mass, if the energy E of the primary can be determined independently [99].

In the HEGRA [25] or BLANCA [22] experiments the primary energy E can be reconstructed from the shower size N_{e} measured with the scintillator array, combined with the Cherenkov observation which removes the A dependence in N_{e}. Alternatively the observation of the Cherenkov light intensity alone leads to an energy determination, for which experimental methods are established. Finally the $X_{\max}$ dependence of the energy E is compared with simulation predictions (see figure 14).

It should be noted, elegant as the Cherenkov experiments may appear, that they infer the elemental composition from only a few observational parameters, essentially of one single EAS component.

2.2.7. Fluorescence light observation. For the experimental EAS research at primary energies above 10^{17} eV there is an efficient method applicable, which allows the measurement of the longitudinal development of the EAS by air fluorescence observation. The technique relies on the fact that ionizing particles can excite N_2 molecules in the atmosphere. Such excited molecules emit fluorescence photons (typically within 10–50 ns after excitation). The optical fluorescence comes from various bands of the molecular nitrogen ion, with light emitted between 3000 and 4000 Å. It happens to be just the wave band for which the atmosphere is quite transparent. The attenuation length is approximately 15 km for vertical incidence. The fluorescence light production efficiency per shower particle is weakly dependent on pressure and temperature. An EAS of 10^{17} eV has more than 100 million electrons at the shower maximum, so that many fluorescence photons are generated, even with a fluorescence efficiency of only 0.5%. The fluorescence light is isotropically emitted and can be detected at large distances from the shower axis. Thus it can be distinguished from air-Cherenkov light that is emitted in the forward direction and confined to short distances from the shower axis. The detection problem is to identify the weak light traces, equivalent to a 40 W bulb, flying through the atmosphere in microseconds at several kilometres distance. The effective area for recording showers is very large as compared to the conventional detector arrays and compensates to some extent the low duty cycle resulting from observations only during clear

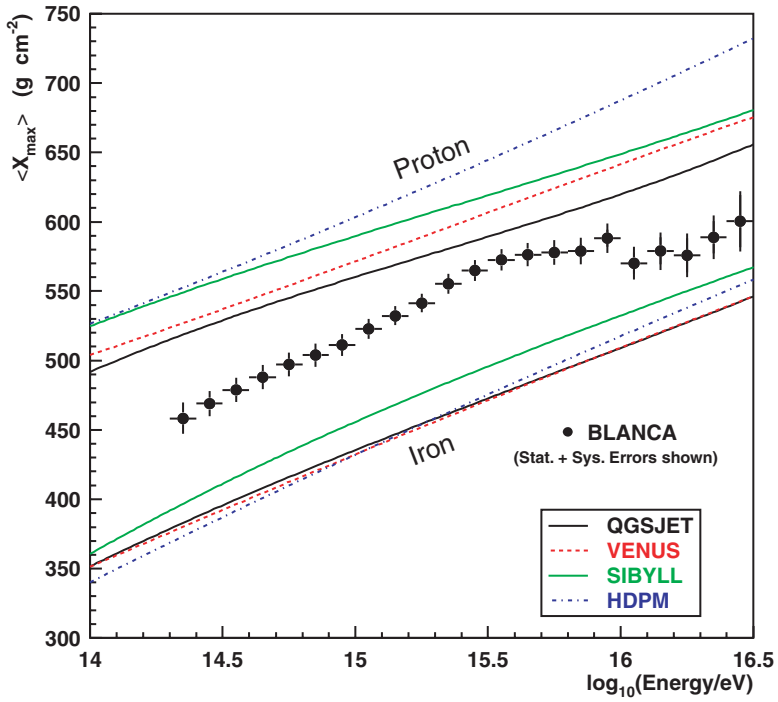

Figure 14. The variation of the atmospheric depth $X_{\max}$ of the EAS maximum from Cherenkov light observations of the BLANCA experiment [22] compared with the predictions of various interaction models.

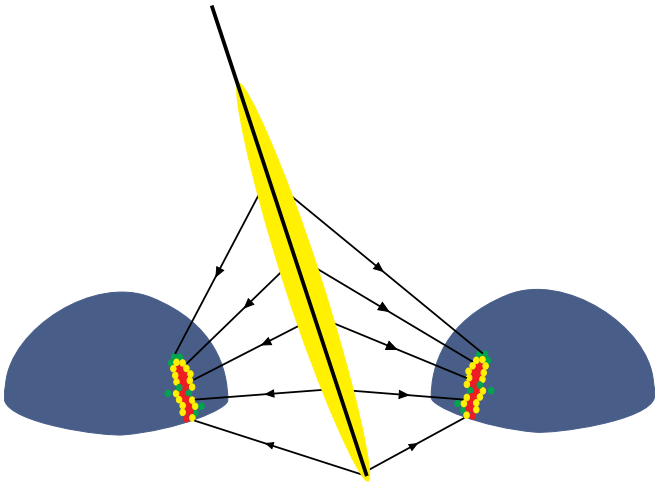

Figure 15. Schematic fluorescence detector assembly for stereo observation [101].

dark moonless nights. There are special techniques used for discrimination against night sky background and terrestrial sources of light noise (aeroplanes, lightning).

Figure 15 sketches the arrangements of two 'eyes' for stereo observations of EAS air fluorescence. The fluorescence technique has been developed and effectively used by the

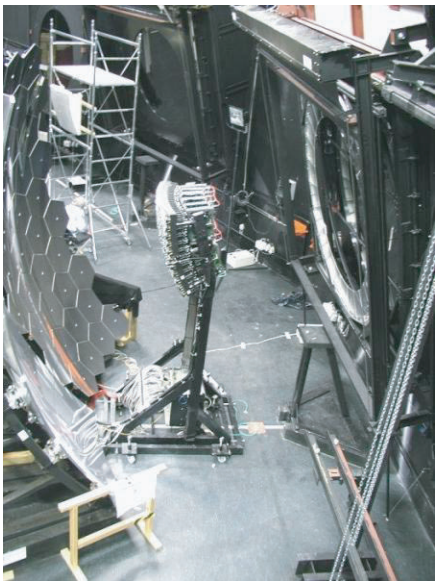

Figure 16. Fluorescence detector assembly for PAO [102].

Fly's Eye detectors, the original Fly's Eye [100] and the extension 'high resolution fly's eye (HiRes-I + II)' [101] installed in Dugway, Utah, 160 km from Salt Lake City, USA.

The fluorescence light is collected using a lens or a mirror and projected onto a camera, located in the focal plane. Essentially the camera is an assembly of a large number of photomultiplier tubes, each looking at a certain region of the sky. The camera pixelizes the image and records the time interval of the light arrival in each pixel element. Figure 16 displays an air fluorescence telescope [102] installed as a part of the Pierre Auger observatory (PAO) [12] in Argentina for studying the highest energies. The detector is a large area spherical mirror telescope of 11 m^2 collecting area of aluminium segments, assembled with a correcting lens (Schmidt optics), covering a field of $30^\circ \times 30^\circ$. The camera is an assembly of 20×22 photomultiplier tubes in the focal plane. The light trace is stored by digital sequences of 100 ns width.

Figure 17 shows the registered light trace of an air-shower particle, seen in 5.9 km distance in the Argentinian Pampa recorded by the Auger prototype telescope at the inauguration of the PAO in June 2001. From such traces together with additional timing information, or more accurately by a stereoscopic procedure using two telescopes, the longitudinal development (shower profile) of the extended air shower in the atmosphere can be reconstructed. The depth $X_{\max}$ of the shower maximum is sensitive to the primary mass ($X_{\max} \propto \ln(E_0/A)$). The track length integral provides a calorimetric measure of the energy. It needs a calibration which involves necessarily a series of careful studies of the light production and transmission in the atmosphere (with monitoring of the actual atmospheric conditions), finally involving also some unknown dependence arising from the particle production model at the highest energies. Actually the insufficient knowledge of the fluorescence yield has turned out to be an important uncertainty in the calibration [103].

2.2.8. Radio emission. Radio emission observation from EAS as an experimental technique of EAS investigations is still in its infancy though the effect was established in 1965 by an

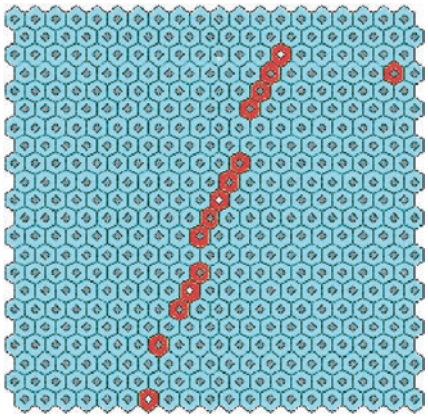

Figure 17. An EAS appears as a trace of illuminated pixels (photomultipliers). The line of the illuminated pixels determines the plane containing the detector and the EAS. In stereo observations by two fluorescence detectors at different sites the intersection of the two detector-EAS planes fixes the EAS geometry.

array of dipole antennas operated in conjunction with Geiger–Müller counters [17, 104]. Even basic questions about the phenomenon and about the interpretation in terms of the properties of primary cosmic rays are not yet clarified. Nevertheless a recent revival of interest has occurred in the context of the progress of modern information technology. The status and the favourable aspects for arrays of large field of view have been discussed by Falcke and Gorham [105] with respect to the project low frequency array (LOFAR) which is a planned astronomical installation of a digital radio telescope. It is intended to combine a single LOFAR like station (comprising about 100 dipoles) with a running standard array like KASCADE: LOPES (LOFAR prototype station). First results are expected in 2004.

2.3. Signatures for energy estimation and mass discrimination

Strictly, the determination of the primary energy and of the mass composition of cosmic rays is an entangled problem. As indicated in the discussion of various observables there are approximate energy identifiers (nearly mass independent) tailor-made for some particular detector installations like the truncated muon number N_μ^{tr} for KASCADE or $S(600)$ for the Haverah Park and AGASA. Principally the signatures for the primary energy and the primary mass of an observed EAS are interrelated. All signatures are based on a snapshot of the actual status of the development of different EAS components at observation level or on some direct information on the longitudinal EAS profiles. The EAS development depends simultaneously on the primary energy as well as on the primary mass, and in a different way (on average) for different EAS components.

The most powerful quantity measured by ground arrays providing information about the primary mass is the correlation between the electron size and the muon content of the EAS (figure 18). With increasing mass of the target or projectile the cross-sections of nucleus–nucleus interactions increase. For example, the inelastic cross-section $\sigma_{\mathrm{inel}}^{A\text{-Air}}$ of iron is at 1 PeV approximately six times larger than for protons of equal energy. Hence an EAS starts and develops earlier, on average, in the atmosphere with increasing primary mass. In a first good approximation a primary nucleus of mass A and energy E_0 can be regarded as a swarm of A independent nucleons generating A superimposed independent proton showers of the

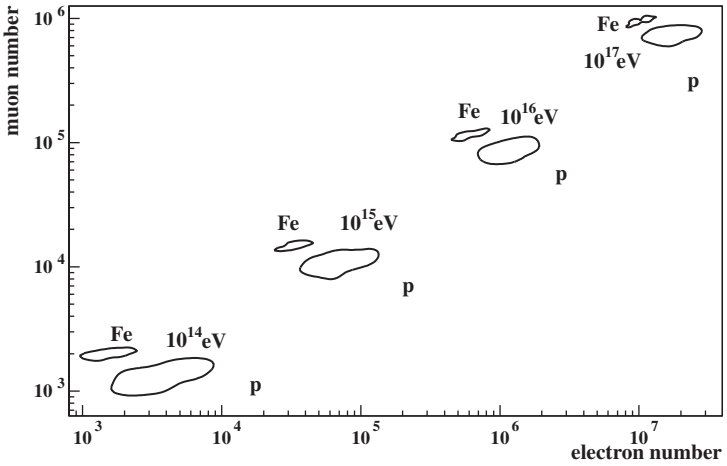

Figure 18. The (N_μ,N_e)-correlation from MC simulations shown for proton and iron primaries at various energies. The lines represent the half-width maxima of the distributions (courtesy of Heck, KASCADE collaboration).

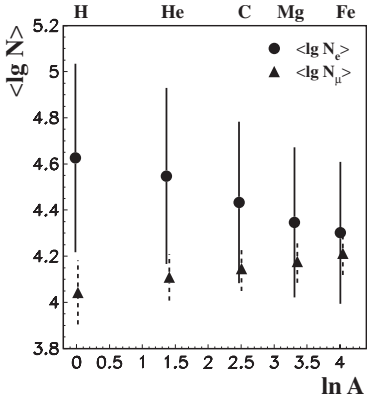

Figure 19. Dependence of the EAS particle numbers N on the primary mass. The error bars represent the fluctuations for 50 simulated EAS observed at sea-level. The simulations refer to CORSIKA [15] for the energy range 1–1.78 PeV and zenith distance $\Theta \in [0^\circ, 42^\circ]$.

energy E_0/A (superposition principle). Thus as a consequence showers induced by heavy primaries generate more secondary particles, each of smaller energy and leading to an earlier attenuation of the electromagnetic component (after the EAS maximum). Simultaneously the number of muons is larger. The muons interact weakly with the atmosphere, they are less absorbed and their decay time is long compared to pions, so that they add up throughout the shower development. Even if the principle is an approximation, this dependence is sufficiently valid. For illustration figure 19 displays the dependence of the sizes of the electron and muon components (simulated for a case of sea-level observations). For statistical reasons the fluctuations of the sum of A independent showers are expected to be smaller than those of a shower generated by a single proton of higher energy, which is experimentally confirmed.

A signature based on observations of the EAS profile is the lateral distribution of air-Cherenkov light, which carries information on the height of the EAS maximum $X_{\max}$

(see section 2.2.6). It has to be combined with additional information in order to disentangle information on energy and mass.

The most important signatures considered for inference of energy and mass are the following:

- The correlation between shower size N_e with the muon content N_μ: the weak dependence of the multiplicity n of the secondaries on the energy of the interacting nucleon, i.e. $n_A(E) \propto A \ln(E/A)$ leading to more secondary particles for heavy primaries combined with the earlier longitudinal development of showers induced by heavy primaries, is the basis of the electron–muon correlation method and its variants. Due to the shorter interaction length and the smaller energy per nucleon and because of the reduced attenuation of the muon component, the electromagnetic component of a heavy-particle induced shower has progressed more on average at the observation level, and the shower carries more muons than a proton induced shower of the same energy.
- The structure of the energy and lateral distributions of muons and hadrons in the shower core: proton induced showers have smaller deflection angles, different production heights, and a harder energy spectrum of the secondaries as compared to heavy ion induced showers of the same primary energy.
- The distributions of the relative arrival times and angles of incidence of the muon component: differences of the longitudinal development and of the mean production height of the muon component are mapped.
- The underground observation of the muon lateral distribution (so-called muon bundles): the spectra and lateral distributions of high-energy EAS muons show differences for different primary masses.
- The observation of the pulse shape and lateral distribution of the air Cherenkov light: the mapping of the longitudinal EAS profile (depth X_{max} of the EAS maximum) by the arrival times and lateral distribution of the Cherenkov photons exhibit a mass dependent sensitivity.
- The observation of the N_2 fluorescence light: the shower profile, the shower maximum X_{max}, and the track length integral are deduced by a calorimetric measurement.

The application of these discrimination signatures will be illustrated with a number of typical experiments.

3. Analysis techniques

The understanding of measured data is closely related to the study of stochastic as well as systematic uncertainties and fluctuations and needs a careful consideration when inferring physical quantities from observations. The stochastic character of the huge number of cascading interactions in the shower development implies considerable inherent shower-to-shower fluctuations of the experimentally observed EAS parameter, clouding the properties of the original particle. As an example figure 20 illustrates strong fluctuations of the electron size N_e at $1000\,\mathrm{g\,cm^{-2}}$ as well as a huge spread in the X_{max} distribution. These inherent fluctuations establish an important and intriguing difficulty of any EAS analysis. They limit approximations by averaging parameterizations and need adequate response by the analysis methods. Moreover the reconstructed electron size N_e^{rec} measured by a scintillator array need not to be the true one, N_e^{true}, and the bias might be energy dependent. Inferring the mass or energy of primary cosmic rays implies a proper treatment of the exemplary uncertainties mentioned above.

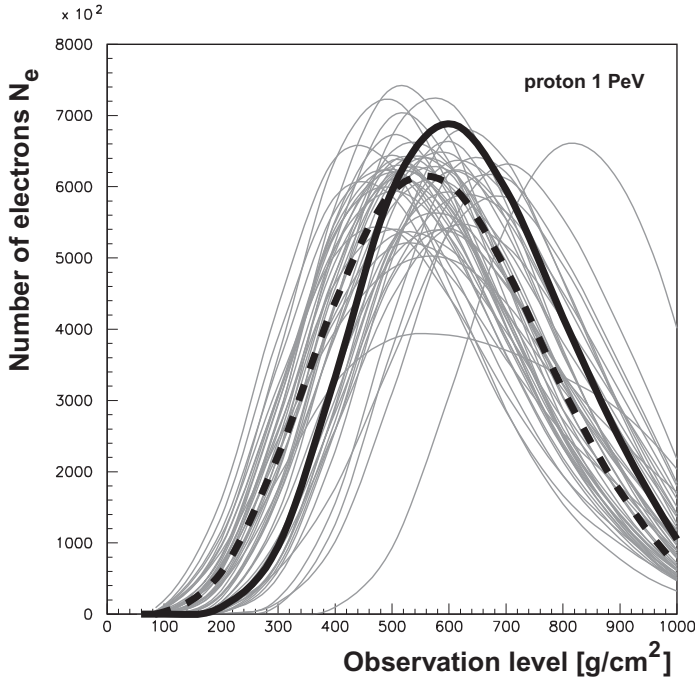

Figure 20. Fluctuations of the longitudinal development of 50 (simulated) proton induced 1 PeV EAS of vertical incidence. An important reason is the fluctuation of the starting depths. The solid thick line represents a shower with an average shower size N_e of the sample at sea level, the dashed line a shower with an average X_{max}.

In general the process of measuring distributions $g(\boldsymbol{y})$ of physical observables $\boldsymbol{y} = (X_{max}, N_e, N_\mu, \ldots)^T$ is often disturbed by inherent limitations, which lead to the non-trivial problem of inferring true distributions from measured ones. Confining conditions like limited acceptance or efficiency of the detector arrangement, finite resolution, strong intrinsic fluctuations and parameter transformations have to be taken into account to solve the inverse problem. Any attempt to determine the energy spectrum and/or the mass composition of CR has to face this fact and congruously deconvolute the systematic effects. As will be seen many trials break off with simplified averaging parameterizations, e.g. neglecting the fact of strong fluctuations which might lead to biased results.

3.1. Analysis scheme

The general scheme of inference in a modern EAS experiment is displayed in figure 21, indicating also the involved difficulties. At best one has to rely on simulated patterns to describe the complex transformation from primary parameters E and A to measured quantities. The identification of differences in EAS which result from differences in mass of the primary particle requires a modelling of the shower development in the atmosphere. For this purpose MC simulation programs of the EAS development like CORSIKA [15], MOCCA [81], AIRES [106] and others have been developed. A prerequisite for MC procedures is the knowledge of particle production in high-energy hadronic interactions, e.g. cross-sections, the multiplicity, the rapidity and p_t distributions and the inelasticity of the multi-particle production in hadron collisions. Since the energy region of interest exceeds by far the particle

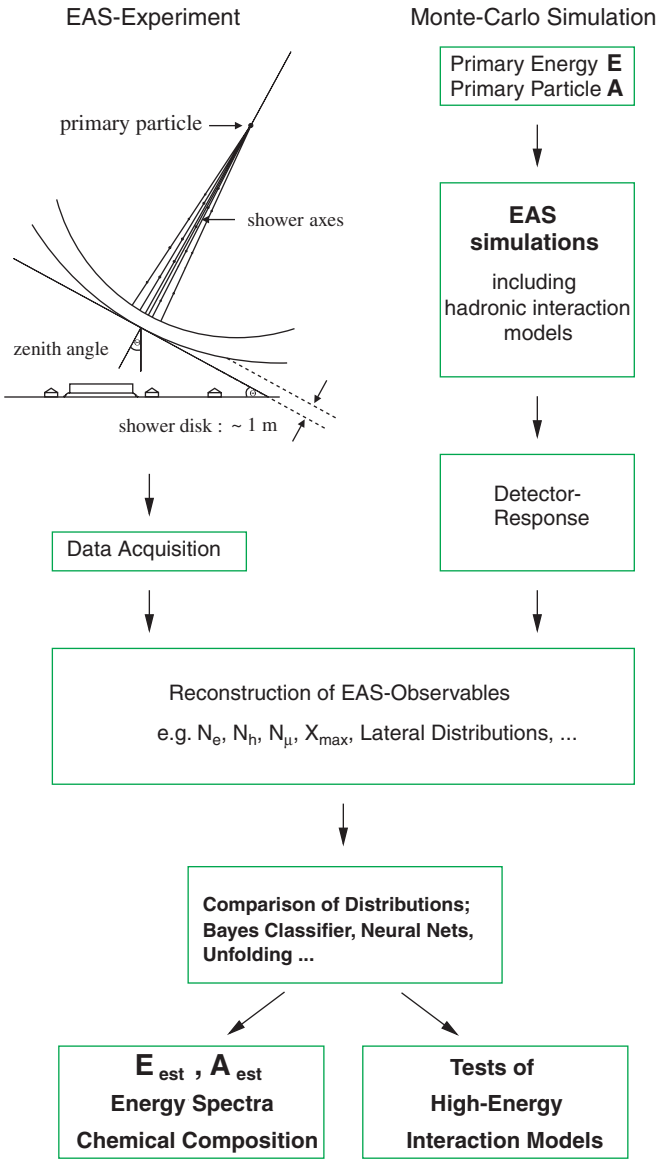

Figure 21. General scheme of the analysis of EAS observations.

energies available at man made accelerators, one has to rely on model descriptions which extend the present knowledge to a *terra incognita*, on the basis of more or less detailed theoretical approaches of phenomenological nature and with QCD inspired ideas (see, e.g. [107, 108]). For example the CORSIKA code includes various models, presently *en vogue*, as options, and in fact, the model dependence is a pronounced feature in the current comparisons with the experimental data.

Further processing compares real data with pseudo-experimental data on an equal level of reconstruction, including the detector response and expressed by various shower variables

like the particle density, multiplicity, lateral spread, arrival time and eventually energy distributions of various EAS components. This desirable procedure is consequently attempted by KASCADE.

3.2. Inference or treatment of an inverse problem

Several approaches are traditionally used to solve the inverse problem of energy and mass deconvolution which in general may be divided in two main classes. On the one hand event-by-event methods exert statistical pattern recognition tools which try to estimate conditional probabilities $p(\omega_i|\boldsymbol{y})$ to associate an observed event $\boldsymbol{y}$ to a certain class ω_i, e.g. ω_i represents the class of primary masses {p, He, C, Fe, ...} (see, e.g. [109]). On the other hand various unfolding procedures are used to infer spectra and elemental composition in terms of frequencies and relative abundances. Both approaches are examined in the following subsections.

3.2.1. Unfolding analyses. Unfolding algorithms to infer physical quantities can be written in terms of Fredholm integral equations of the 1st kind

$$g_i(\boldsymbol{y}) = \int_0^\infty t_i(\boldsymbol{y}|x)\, j_i(x)\, \mathrm{d}x, \tag{12}$$

where the transfer function $t_i(\boldsymbol{y}|x)$ has to cover all the above-mentioned limiting effects and is realized by means of detailed MC simulations for each individual primary mass ω_i under consideration to describe the measured size spectrum $g(\boldsymbol{y}) = \mathrm{d}n/\mathrm{d}\boldsymbol{y}$ with

$$g(\boldsymbol{y}) = \sum_i g_i(\boldsymbol{y}). \tag{13}$$

Various mathematical methods and variants of unfolding procedures exist to determine the intensity distribution $j_i(x) \propto \partial n_i/\partial x$ of the energy $x = E$ or any shower size $x = N$ for different masses ω_i and might be categorized as detailed below:

(a) A plain solution: as mentioned above, one type of analysis is based on comparisons by use of a plausible *a priori* parameterization of an averaged one-dimensional distribution y, introducing some constraints by analytical expressions and neglecting inherent fluctuations. The transfer function is then a simple delta-distribution $\delta(x - x_0)$ times the Jacobi matrix, i.e. the matrix of partial derivations, to transform the intensity spectrum of an individual mass ω_i from one into another size distribution

$$t_i(y|x) = \delta(x - x_0)\, \left.\frac{\partial x}{\partial y}\right|_{\omega_i}.$$

As an example the graphs in figure 22 display the averaged energy estimate as a function of the simulated energy $x = \lg E_0$. In both cases the energy estimate $y = \lg E_{\mathrm{est}}$ is a composition of electron and muon size observables. Even though the estimated energy is unbiased on average there is undoubtfully a bias when an all-particle energy spectrum is inferred, because shifts in the energy estimation due to the convolution of a steep falling power-law spectrum and the energy resolution (e.g. a log-normal distribution) are neglected

$$g_i(y) = \int_0^\infty t_i(y|\lg E)\; j_i(\lg E)\; \mathrm{d}\lg E = \left.\frac{\partial \lg E_0}{\partial y}\right|_{\omega_i} j_i(\lg E_0). \tag{14}$$

Different energy resolutions for different primaries disturb the picture additionally. The reconstructed spectrum results in an overestimation of intensities and a biased slope γ, if the mass composition changes with energy. Even so, the application of this approximation

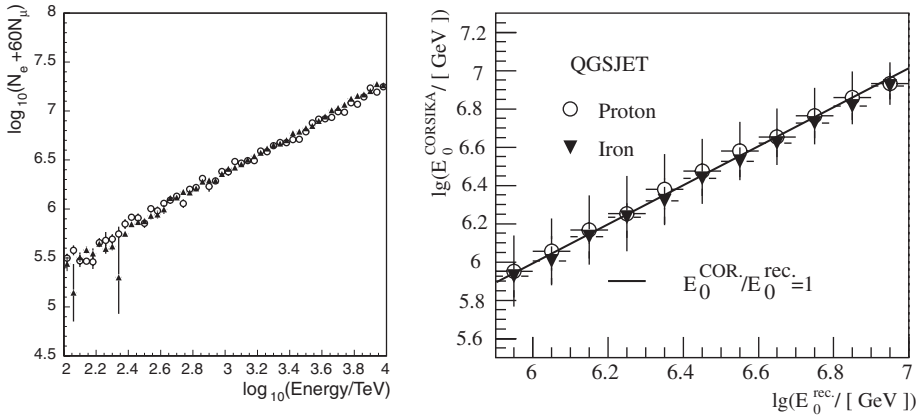

Figure 22. Left: the CASA-MIA [20] energy parameter $\lg(N_e + 60N_\mu)$ as a function of energy for protons (○) and iron (▲). Right: energy calibration curve of KASCADE data by Weber *et al* [110]. The energy is parameterized as a function of N_e and N_μ^{tr}.

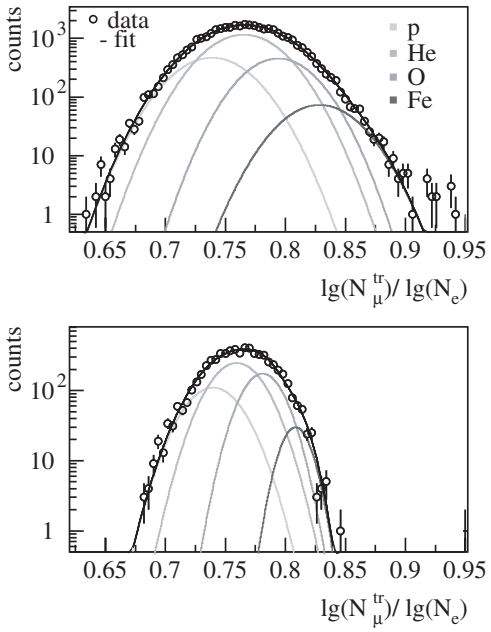

Figure 23. The muon/electron ratio for two different energy intervals determined by KASCADE [110] (top: $6.2 \leqslant \lg(E/\mathrm{GeV}) < 6.3$; bottom: $6.7 \leqslant \lg(E/\mathrm{GeV}) < 6.8$). The simulation distributions are approximated by Gaussian functions.

gives a fairly simple estimate for the slope of the energy spectrum $\gamma_i = \alpha_i(\beta - 1) + 1$, by assuming $j_i(E_0) \propto E_0^{-\gamma_i}$, $g(y) \propto y^{-\beta}$ and $y|_{\omega_i} \propto E_0^{\alpha_i}$ which is of course in general different for different primary masses ω_i.

(b) A simplified multi-dimensional analysis: more refined methods also make use of fluctuations of observables and are often parameterizations of one-dimensional projections. Figure 23 displays measured and simulated $\lg N_e / \lg N_\mu^{tr}$-spectra of the KASCADE experiment for two different estimated energy intervals. Despite the fact that the estimated energy (i.e. see right graph in figure 22) itself is subject to biases due to the aforementioned notes,

the determination of the elemental composition is performed in a more complex manner. The simulated distributions $y = \lg N_e / \lg N_\mu^{tr}$ are parameterized as normal distributions and the normalization factors are fitted to the measured distribution of equation (13). Hence the transfer function can be written in the following form

$$t_i(y|E) \propto \frac{1}{\sqrt{2\pi\sigma_{E,i}^2}} \exp \frac{(y - \langle y \rangle_{E,i})^2}{2\sigma_{E,i}^2}. \tag{15}$$

Albeit energy and mass dependent fluctuations $\sigma_{E,i}$ are accounted for, part of the correlations between the observables are omitted due to the projection. Another example of such an unfolding procedure by the HEGRA experiment [111, 112] is shown in figure 24 (left). The elemental composition is estimated by comparisons of the X_{max} distribution, where two simulated primary groups are histogrammed and fitted to measured data. The energy scale is determined independently in figure 24 (right). Again the fluctuations are taken into account, but one assumes no cross-talk between different energy and mass related observables.

(c) Sophisticated multi-dimensional analysis: if equation (12) has to be solved using various observables simultaneously as well as their correlations several problems occur. For example it is known that a well-behaved solution does not necessarily exist for equation (12) when arbitrary well-behaved functions $t(\boldsymbol{y}|x)$ and $g(\boldsymbol{y})$ are prescribed [113]. Moreover the existence of a solution of equation (12) does not imply uniqueness. Namely, if $j_i(x)$ is such a solution, then $q_i(x) = j_i(x) + r_i(x)$ is also a solution, where $r_i(x)$ satisfies the homogeneous equation, i.e. $g(\boldsymbol{y}) \equiv 0$. It is evident that subsidiary conditions are required before uniqueness can be guaranteed. Several methods handle such difficulties [114–116] and introduce restricting conditions like regularization [114] or positiveness of the transfer matrix

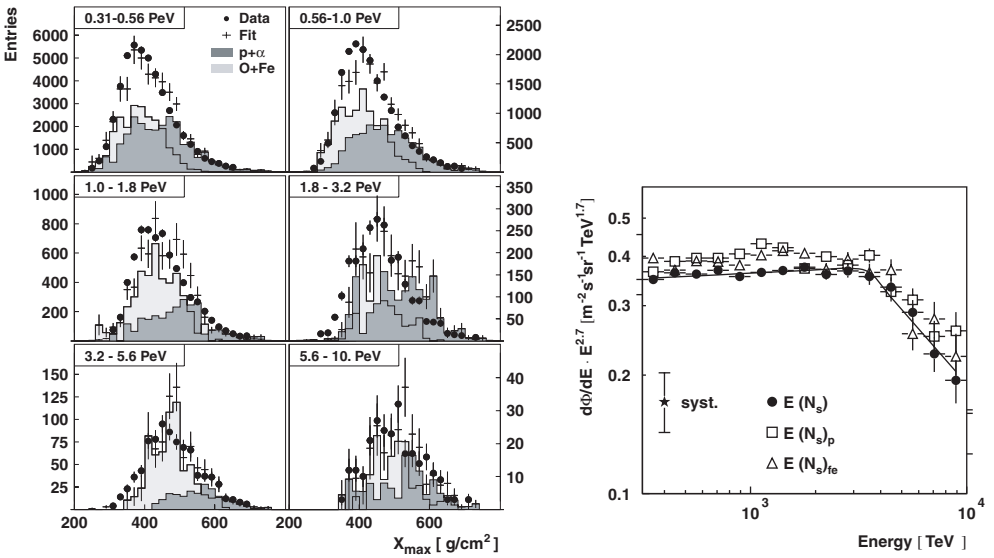

Figure 24. Left: X_{max} distributions (•) of the HEGRA experiment and the fitted distribution of the light (dark shaded) and the heavy mass group (light shaded) for six intervals of reconstructed energy. The crosses denote the sum of the two mass groups with statistical errors [111]. Right: the differential energy spectrum of the HEGRA experiment derived with three different methods. The line indicates a fit to the so-called mass independent $E(N_s)$ spectrum using an averaged transfer function according to a previously determined mass composition. The star indicates their estimated systematic error due to the uncertainty of the energy scale [112].

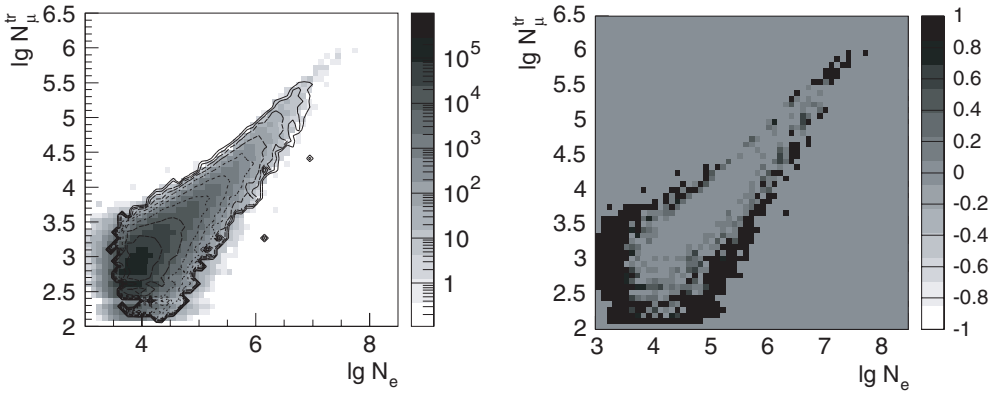

Figure 25. On the left-hand side the two-dimensional (N_e, N_μ^{tr}) size spectrum (grey scale) measured by the KASCADE experiment is compared with the reconstructed distribution (contour). The corresponding difference $(N_{exp} - N_{MC})/N_{exp}$ between experimental and simulated data is shown on the right-hand side [117]; $\theta \in [0^\circ, 18^\circ]$.

t [116] or smoothness of the solution $j_i(x)$ [115]. Figure 25 displays the two-dimensional (N_e, N_μ^{tr}) size spectrum measured by the KASCADE experiment [117]. After applying an unfolding procedure [115, 117] the reconstructed size spectrum is constructed (contour lines). The comparison of both distributions clearly shows differences which are described by the authors as follows: first of all the lack of MC data at the threshold prevents extraction of the energy spectrum below the threshold energy of about 10^{15} eV. In addition, the limited number of MC simulations does not allow us to describe the regions of small statistical accuracy. Especially a band along the proton region occurs (lower bound of the contour) reflecting the fact that protons have large fluctuations which are not well reproduced by the statistical limitations of the MC simulations.

Despite the intricate features encountered it is obvious that the information content which is provided by the measurements is accounted for in a nearly optimal way. In general it should be remarked that the information content of two- or multi-dimensional projections is clearly larger than that of one-dimensional ones. The latter is obvious because multi-dimensional distributions determine one-dimensional projections on the coordinate axes unambiguously whereas there are infinitely many multi-dimensional ones which reproduce a given set of marginal distributions.

Unfortunately the lack of statistical accuracy of MC data often prevents use of multi-variate tools and one is restricted to more simple approaches, losing resolution power and quantitative reliability of the results. The so-called curse of dimensionality [118], especially, limits the simultaneous analysis of a larger number of observables when the size of MC samples is too small. The dimension m of the random vector $\boldsymbol{y}$ is limited in the case of a finite set of random samples by the following condition: when considering each component of an m-dimensional observation vector by M divisions (bins), the total number of cells is M^m and increases exponentially with the dimensionality of the input space. Since each cell should contain at least one data point this requirement implies that the size of training samples (or reference pattern samples) needed to specify the non-parametric mapping, increases correspondingly.

3.2.2. Event-by-event analysis. In contrast to unfolding methods mentioned before, the objective of multi-variate event-by-event analyses is not to deconvolute effects caused by the

transfer function t, but to assign for each individual occurrence $\boldsymbol{y} = (X_{\max}, N_e, N_\mu, \ldots)^T$ an *a posteriori* probability $p(\boldsymbol{y}|\omega_i)$. Hence a multi-dimensional event is associated to a particular class, e.g. $\omega_i \in \{\mathrm{p}, \mathrm{He}, \mathrm{C}, \mathrm{Fe}, \ldots\}$ including mis-classification which has to be taken into consideration when abundances are calculated.

Pattern recognition, or decision-making in a broader sense, may be considered as a problem of estimating density functions in a multi-dimensional space and dividing the space into the regions of categories or classes. It can be theoretically shown in terms of statistical hypothesis testing that the best classifier is the so-called Bayes classifier which minimizes the probability of classification error [119]. Other event-by-event classifiers and estimators like neural networks [118], etc cannot outrun the Bayes classifier, not even in principle. For this reason only Bayesian decision-making is briefly described below.

The method is based on the Bayes theorem [120]

$$p(\omega_i|\boldsymbol{y}) = \frac{p(\boldsymbol{y}|\omega_i) \times P(\omega_i)}{p(\boldsymbol{y})} \quad \Leftrightarrow \quad \text{posterior} = \frac{\text{likelihood} \times \text{prior}}{\text{normalization factor}} \tag{16}$$

with $p(\boldsymbol{y}) = \sum_{j=1}^{N} p(\boldsymbol{y}|\omega_j) P(\omega_j)$, which holds if the different N hypotheses ω_i (i.e. classes) are mutually exclusive and exhaustive. By a prior and a normalization factor the theorem connects the likelihood of an event $\boldsymbol{y}$ of a given class ω_i with the probability of a class ω_i, being associated with a given event $\boldsymbol{y}$. The prior gives the *a priori* knowledge of the relative abundance of each class and is major basis of debates on Bayesian inference procedures and is often determined by iterative methods or, even simpler, by inverting a mis-classification matrix.

In the fortuitous case that the likelihood functions $p(\boldsymbol{y}|\omega_i)$ are known for all populations, the Bayes optimal decision rule is to classify $\boldsymbol{y}$ into class ω_i, if

$$p(\omega_i|\boldsymbol{y}) > p(\omega_j|\boldsymbol{y}) \tag{17}$$

for all classes $\omega_j \neq \omega_i$.

Such predictions $p(\omega_i|\boldsymbol{y})$ hardly exist as an analytical formula in CR physics, one has to rely on MC data and build up estimates for these likelihood functions. Fashionable estimators are non-parametric Kernel-estimates like the Parzen density estimate [121] or the k-nearest neighbour (kNN) density estimate [119] and applied by the KASCADE [122] and CASA-MIA [20] experiments, e.g. in the latter approach the density function is estimated

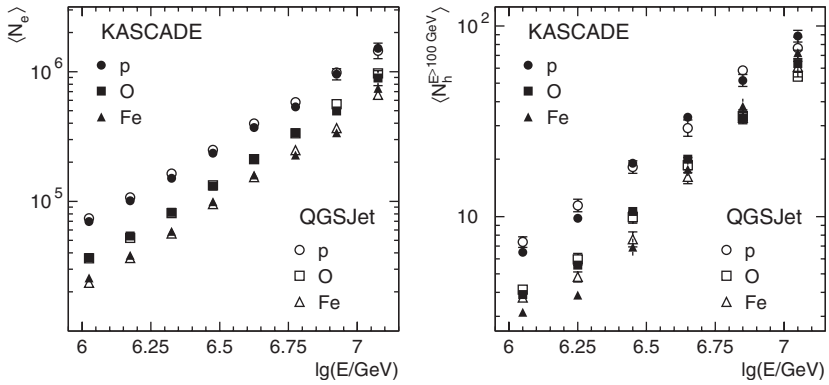

Figure 26. The projected relations $\lg N_e$ and $\lg N_h^{E>100\,\mathrm{GeV}}$, respectively, vs $\lg(E/\mathrm{GeV})$ from a non-parametric analysis, trained to estimate the energy and mass of the measured events using N_e and N_μ^{tr} as EAS observables.

locally by a small number of neighbouring samples without a parameterization of the underlying distribution. Due to the event-by-event assignment, model tests concerning observable correlations can be performed quite naturally and without *a priori* parameterization. As an example figure 26 displays on the left-hand side the relation between electron size N_e and energy E for KASCADE data [122], which shows no difference between simulated and measured samples of individual mass groups. Of course, this is not surprising, since the pattern recognition tool (i.e. a neural network) is just trained in such a way that deviations, incompatible with the statistical accuracy, would cast some methodical doubts on the algorithms used. More remarkable is the agreement of the hadron number $N_h^{E>100\,\mathrm{GeV}}$ (which was not included in the determination of $p(\omega_i|\boldsymbol{y})$) vs primary energy, found by the same tool though with larger fluctuations of the mean values. That may be explained by the reduced mass sensitivity of $N_h^{E>100\,\mathrm{GeV}}$ and the dominance of the (N_e, N_μ^{tr})-correlation.

3.3. Remarks about multi-variate analyses

For the comparison of the measured observables with the pseudo-data we have to realize that none of the observables is strictly dependent only on the mass of the primary, or dependent only on the energy. Since we are investigating an *a priori* unknown spectral distribution accompanied by another *a priori* unknown variation of the elemental composition (or vice versa), there is always an intriguing feedback of the estimates of both. Therefore multi-variate analyses, correlating the observations of different EAS variables, are strongly required, and the inference from only one single EAS component, e.g., is shown to be often misleading.

It should also be emphasized that a multi-detector experiment observing simultaneously all major EAS components with many observables provides some good possibilities to test the hadronic interaction models and to specify the most consistent one [122]. Actually this is another facet of the high-energy cosmic ray observations which cannot be disentangled from the astrophysical implications of EAS observations: looking for information on the hadronic interaction up to energy regions which may never get explored by artificial accelerators.

As the limited statistical accuracy (curse of dimensionality) prohibits the simultaneous (multi-variate) analysis of a larger number of EAS observables, when the size of training samples is too small, one has to restrict himself to more simple approaches. None the less if correctly stated and accounted for, systematic biases can be avoided.

We conclude that there are obviously methodical uncertainties in the analyses when comparing results of different experiments. This fact is actually often the reason for controversial debates and demands a careful statement about the methodical accuracy of reported results.

4. Energy spectrum and mass composition in the knee region

In their first conclusion in 1958 the discoverers of the knee claimed that the kink in the spectrum is a consequence of the superposition of cosmic rays of galactic and super-galactic origin [1]. Two years later Peters pointed out with a theoretical argument that the position of the knee should get shifted in proportion to the charge of the primaries if magnetic fields were responsible for the acceleration of the cosmic rays [123]. Nowadays it is believed that cosmic rays are accelerated in a process called diffusive shock acceleration. Suitable astrophysical shocks occur in supernova explosions, and ionized nuclei gain energy as they are repeatedly overtaken by the expanding shock wave. Such mechanisms (see, e.g., [124, 125]) lead in fact to a power-law spectrum with a maximum energy of about $Z \times 10^{15}$ eV, which roughly agrees with the observed steepening (though the theoretically predicted spectrum proves to be

steeper than actually observed). More detailed calculations for the expected energy spectra at Earth by a cut-off at the acceleration [126, 127] agree within the all-particle spectrum, but result in considerable differences for the spectra of the various particle masses. Accidentally, an explanation of the knee by the (rigidity dependent) propagation of the cosmic particles in the galactic magnetic field (leakage box model) [128] leads also to a change of the spectral index due to the decreasing containment and rising leakage with increasing rigidity of the (light) particles and can explain the measured all-particle spectrum [129, 130]. An interesting hypothesis about the origin of cosmic rays around the knee has been propagated by Erlykin and Wolfendale [71, 131], predicting a modulation in the energy spectrum, i.e. structures (wiggles) due to the various mass production spectra of a single supernova source, localized only few hundred light years away from our solar system. Alternatively to such astrophysical reasons, a sudden change of the character of the hadronic interaction at higher energies has been proposed as explanation of the knee [132, 133]. Such speculations are fed by conspicuous (to date not yet disproved) observations of a drastic change of EAS size spectrum at very high altitudes (see figure 7). Also models adopting new channels of the primary interaction with relic neutrinos [134] or transformation of energy into gravitational waves [135] are on the market. The validity of such models based on particle physics as explanation of the knee will be most probably proved or disproved by the new generation of accelerators like the Large Hadron Collider (LHC), presently being built at CERN.

In order to constrain the various models and conjectures an improved and detailed knowledge of the shape of the energy spectrum around the knee is very important. In particular, all approaches accounting for the origin and acceleration mechanism imply specific variations of the elemental composition of primary cosmic rays, sometimes in a very complex manner.

4.1. The energy spectrum

The basic idea for deducing the primary CR energy spectrum around the knee from EAS observations is to carry out a calorimetric determination of the energy of shower cascades, e.g. by the total Cherenkov light intensity produced in the atmosphere or by the total number of (charged) particles at a certain observation level. The determined quantities are related to the primary energy. In general, they depend unfortunately also on the (unknown) mass of the primary and further information, which needs necessary assumptions to account for this dependence. Typical examples of such measurements are the energy spectra obtained by the Akeno [31] and Tibet [39] detector arrays. Both experiments use a field of scintillation detectors to measure the charged particle component. Akeno converted the obtained size of the showers into the primary energy by the help of EAS results measured at observation levels at high altitude (conversion in the shower size N_e^{max} at the maximum) and a theoretically anticipated parameter for the dependence of the shower size maximum on the primary energy. The Tibet experiments use MC simulations for fitting the obtained size spectrum, introducing the elemental composition as free parameter. The two energy spectra from the two different experiments (see figure 27) disagree in the position and the sharpness of the knee: Akeno attained a much sharper knee at a higher energy position than the results of the Tibet experiment. Such differences in the spectral shape are the subject of current discussions.

Figure 27 compiles the energy spectra obtained by various different experiments. Most of them use for the reconstruction of the energy a single observable like the EAS size and convert the obtained size spectrum with the help of MC simulations. In contrast, the multi-detector set-up of the KASCADE experiment, e.g., enables us to determine both the electron and muon sizes for each single EAS event. As a first approximation the quantity $\lg N_\mu^{tr}$ (see section 2.2.2) is used as energy identifier (or a combination with the shower size $\lg N_e$). Strictly, however,

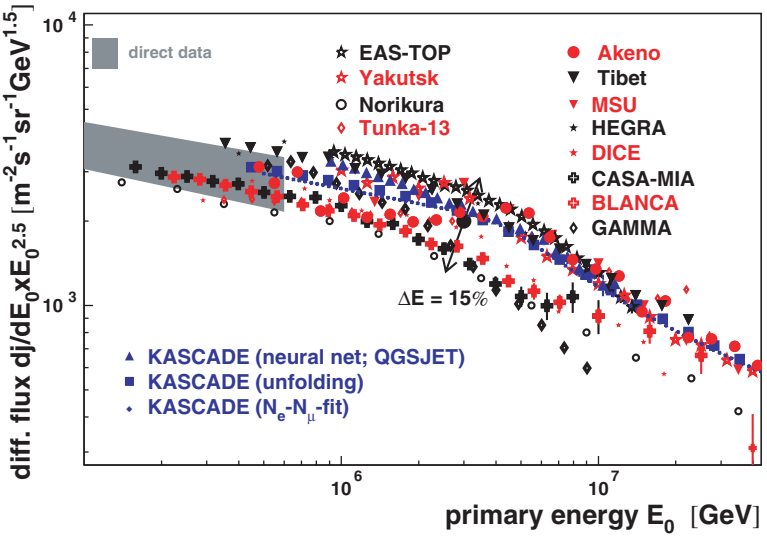

Figure 27. Compilation of different experimental results on the cosmic ray all-particle energy spectrum around the knee (from [136]). The effect of a 15% uncertainty in energy reconstruction is indicated (Akeno [31], Tibet [39], MSU [28], HEGRA [24], DICE [23], CASA-MIA [78], BLANCA [22], GAMMA [38], EAS-TOP [67], Yakutsk [137], Norikura [46], Tunka [51], KASCADE [122, 66, 138]).

the task is to explain simultaneously and consistently the observed electron and muon size spectra by one unique primary energy spectrum. For that purpose various methods have been applied to reconstruct the primary energy spectra in a consistent way using both observables simultaneously. In this section we describe methods without taking into account the correlation of the observables on an event-by-event basis (more sophisticated analyses will be discussed in section 4.3). In this manner the correlated information on energy and mass, just looked for, gets disentangled.

A common fit to the electron and muon size spectra with the assumption of two primary mass group spectra following two power-laws with a knee, leads to the energy spectra of the two components (with a missing knee for the heavy component as main result) and the all-particle energy spectrum as sum [66]. The fit is based on a Fredholm integral equation with the detector response function as kernel. This response function is prepared by detailed MC calculations including a full simulation of the detector properties. An analysis step forward is the application of an unfolding procedure on the two size spectra [138] leading to the mass group spectra of four components. A further analysis using the two sizes per single event is based on neural net estimations of the primary energy [122]. The latter procedure shows the sensitivity to the influence of different hadronic interaction models as the net is trained by two different models (figure 28).

Assuming an uncertainty of 15% for the energy reconstruction (shown in figure 27 at 3×10^{15} eV) all the results presented in figure 27 appear to be concordant. Despite considerable differences of the applied methods analysing the observables, different simulation procedures, and different observation levels the compiled experimental results agree remarkably. Only at the high-energy end do the spectra exhibit larger differences, maybe as a consequence of saturation effects of the different detector devices, in addition to missing statistical accuracy and also due to larger uncertainties of the models providing the reference patterns. This observation is remarkable, in particular as most of the experimental results have been published

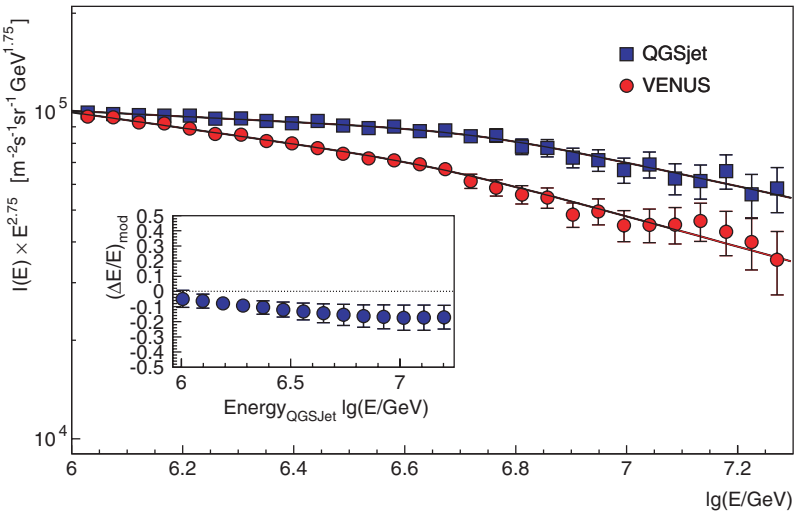

Figure 28. CR all-particle energy spectrum resulting from a non-parametric analysis of KASCADE data [122] with two different hadronic interaction models underlying the neural network training. The inset shows the relative deviations calculated on event-by-event basis of the results using the two models.

without quoting systematic uncertainties arising from the reconstruction procedures or the model dependence.

After compiling the data (14 spectra) the average values and their variances result in a slope below the knee to $\gamma_1 = -(2.68 \pm 0.06)$ and above the knee to $\gamma_2 = -(3.06 \pm 0.08)$ with the knee position at $E_k = (3.2 \pm 1.2) \times 10^{15}$ eV, without taking into account the statistical accuracy of the different experiments or any further systematic uncertainty of the given results. In most cases systematic uncertainties are not communicated for the results shown in the plot.

4.2. The elemental composition

Studies of the mass composition of cosmic rays in the knee region have considered various signatures (see the compilation in section 2.3) and observable combinations, in addition to the application of different reconstruction procedures.

One approach is simply the comparison of the distributions of the mass sensitive observables with MC predictions for different primary masses in energy intervals. Examples of that procedure are the MSU [28] experiment which observes the fluctuations in muon number, or the BLANCA [22] experiment analysing the slope of the lateral distribution of the Cherenkov light as a mass sensitive observable. The left panel of figure 29 shows an example of a common fit of MC expectations to the slope, for various mass groups, of the distribution measured by BLANCA. Another parametric comparison between expectations and data is performed by EAS-TOP/MACRO [139] where the relevant observable is the muon multiplicity measured deep underground (figure 29, right panel). EAS experiments on Mt Chacaltaya [54] consider the hadron multiplicity measured in burst chambers for different shower size ranges. The experimental ratio of the muon content to the electron size as an observable (representing the (N_e, N_μ)-correlation), has been analysed in KASCADE [110] and CASA-MIA [78] by adopting the ratios of the single shower components from predictions of MC simulations (see figure 23).

Figure 30 compiles different experimental results of the quantity X_{max} derived from Cherenkov light observations. It indicates how sensitive the results are to experimental

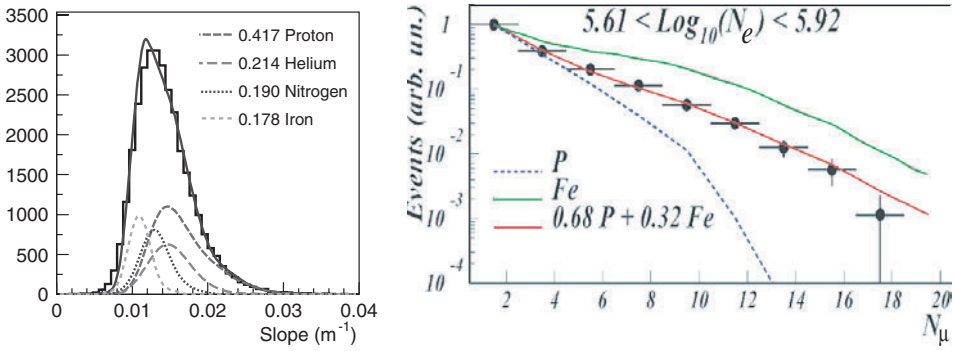

Figure 29. Distributions of mass sensitive observables in the primary energy range of the knee. Left panel: slope of the lateral distribution of the atmospheric Cherenkov light as measured with BLANCA [22] and interpreted as superposition of different components. Right panel: muon multiplicity distribution as measured with the MACRO installation [139] deep underground and compared with predictions of MC simulations.

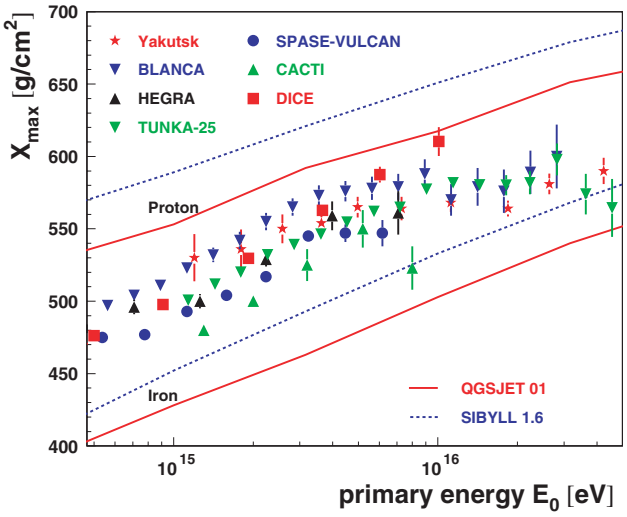

Figure 30. Compilation of different experimental results on the estimation of the shower maximum by measuring the air Cherenkov light (Yakutsk [159], BLANCA [22], HEGRA [24], TUNKA-25 [140], SPASE [48], CACTI [141], DICE [142]). Predictions by MC simulations [15] for two different models are also shown.

uncertainties and to differences of the EAS MC simulations. There are differences up to 40 g cm^{-2} originating from the predictions of different high-energy interaction models as MC generators. Systematic experimental uncertainties may account for fluctuations of the same grammage. This is in addition to the uncertainty of the energy estimation and may explain the scatter of the data points. Thus, on the basis of this observable a definite conclusion on the mass composition is hardly possible.

In recent analyses more attention is paid to systematic uncertainties. The experiment BLANCA, which consists of an array of 144 photomultipliers for the observation of the Cherenkov light, reconstructs the height X_{max} of the shower maximum as the main observable. In a recent publication BLANCA presented a detailed analysis of sources of systematic uncertainties arising from the reconstruction procedure (figure 31).

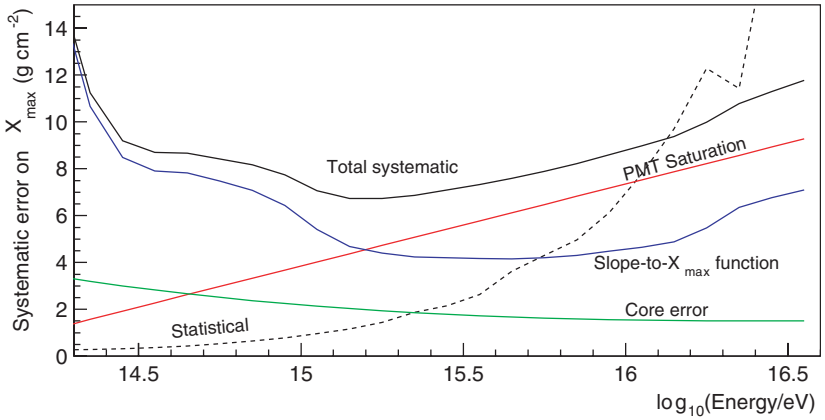

Figure 31. Sources of systematic uncertainties for reconstructing the $X_{\max}$-observable from measurements of the BLANCA experiment [22].

As already emphasized the experimental concept of the KASCADE experiment is a multi-component detector array for measurements of a larger number of EAS observables for each individual event with high accuracy. Specific EAS quantities accessible, in addition to the shower size N_e and the truncated muon number N_μ^{tr}, are the number of hadrons N_h^{100} with energies larger than 100 GeV, the energy sum $\sum E_h$ of the hadrons, the energy of the most energetic hadron E_h^{max} [143], the number N_μ^* of muons with energies larger than 2.4 GeV [85] and others like some quantities relating to longitudinal EAS profile via the temporal structure of the shower disc (muon arrival time distributions [144]) and angles-of-incidence distributions of muons [145]. The (multi-variate) analyses performed by the KASCADE collaboration have revealed that the resulting mean logarithmic mass depends strongly on the particular choice of observables [122]. The same analysis method and procedures (neural net classification always trained with the same set of simulations) have been applied to different sets of KASCADE observables. Figure 32, though displaying similar trends with the energy observable N_μ^{tr}, shows systematic differences in the composition (represented by the mean logarithmic mass) for different observable sets. In particular the resulting composition changes drastically depending on whether the shower size N_e is included in the analysis or not. This feature is considered to be due to the internal inconsistencies of the models used for generating the reference patterns. In fact there is also a noticeable model dependence. In order to smooth the uncertainty of using different observables, averaged values resulting from multi-variate approaches using different observables are displayed for two different interaction models (underlying the neural net training) and are compared to other experimental results in figure 33.

Figure 33 which compiles results of different qualities, gives an impression about the actual situation, whose improvement is limited by the model dependence of the analyses, by the chosen observables, and by experimental systematic uncertainties. In summary most of the results establish the increase of the mean logarithmic mass above the knee position, although on different absolute scales.

4.3. Energy spectra of single mass groups

A more detailed insight into the structure of the knee is provided by the spectra of single mass groups. A rather direct indication of a different behaviour of the light and heavy CR components stems from the KASCADE measurements of the frequency spectra of the local muon density. Muon density spectra have been reconstructed [147] for events measured at fixed

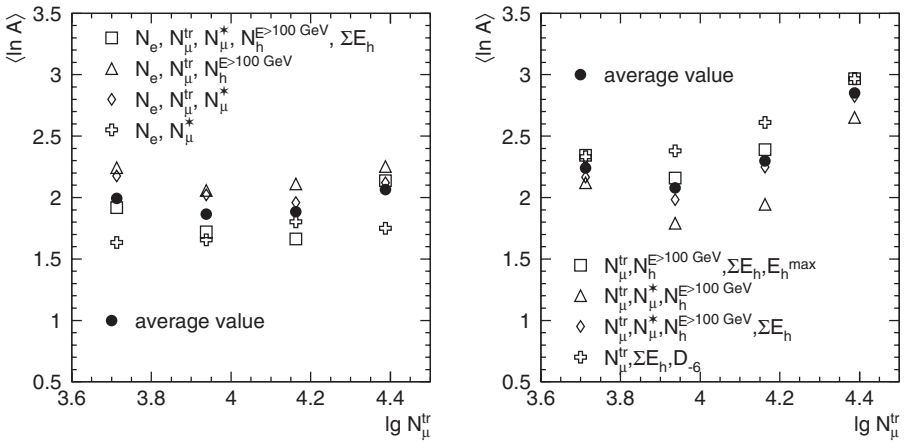

Figure 32. Energy dependence ($\propto N_\mu^{tr}$) of the mean logarithmic mass using different sets of observables in a multivariate approach. Additionally to methodical uncertainties which are quoted to be ≈0.4 in the mean logarithmic mass, systematic differences appear when the EAS electron size is included in the correlation (left panel) or not as in the right panel (from [122]).

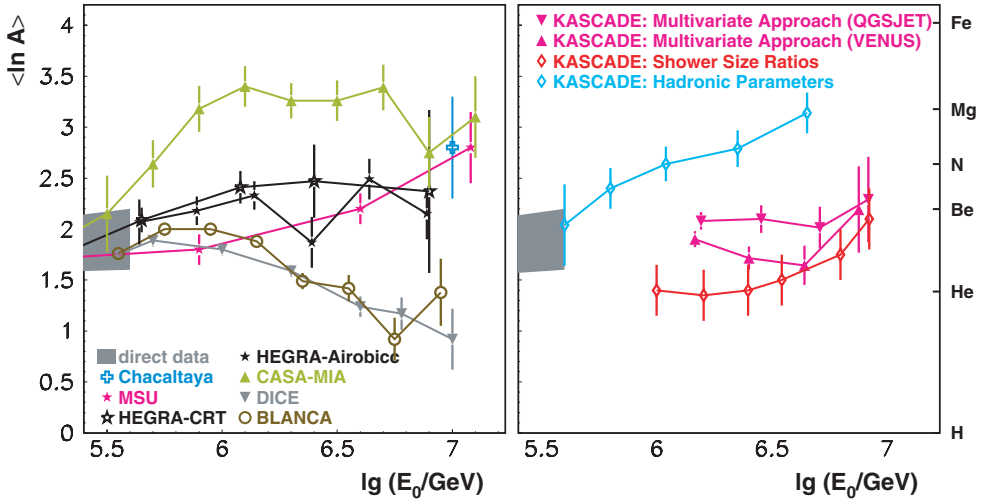

Figure 33. Compilation of different experimental results of the mean logarithmic mass around the knee. Results of KASCADE (right) and other experiments (left) according to the situation in the year 2000. (Chacaltaya [54], MSU [28], HEGRA-CRT [26], HEGRA [24], CASA-MIA [78], BLANCA [22], DICE [23], KASCADE [138, 122, 110, 146]).

distances from the shower axis and for different muon energy thresholds. The event selection has been performed with the help of the scintillator array, whereas the muon densities are determined independently by the devices of the KASCADE central detector. Moreover, the possibility of reconstructing the electron to muon number independently allows us to divide the total sample of EAS in electron-rich (induced by light nuclei) and electron-poor (induced by heavy nuclei) subsamples. This selection is nearly independent of MC simulations and adopts only the assumption that showers induced by light primaries have a larger ratio than EAS induced by heavy primaries (see section 2.3). The analysis reveals the appearance of the knee in the local muon density spectra, quite pronounced in the electron-rich subsample, and

disappearing in the electron-poor subsample (figure 34). The accessible energy range for this analysis covers the energy range between 1 and 10 PeV. The results were found to be valid for many different core distances and for two muon energy thresholds. It is a strong experimental hint for the origin of the knee being a decrease of the flux of only light primary particles.

Measurements of the shower size combined with muon multiplicities measured in a 144 m^2 muon tracking detector at the EAS-TOP experiment indicate also a decrease of the contribution of light primaries to the flux above the knee [148].

A promising way towards a solution of the puzzle of the knee is a new approach worked out by the KASCADE collaboration. The good statistical accuracy and reliable estimates of the electron and muon sizes per single shower allow us to apply unfolding methods to the two-dimensional size distribution and to infer the energy spectra of different mass groups. Mathematically the inverse problem is put as described by the equations (12) and (13) of section 3.2.1 with $\boldsymbol{y} = (N_e, N_\mu^{tr})$ and $x = E$. The response matrix (transfer function) includes, additionally to the mass sensitive shower sizes, also the intrinsic shower fluctuations, which are also mass dependent. The construction of the response function is based on EAS MC simulations. Different methods have been applied to solve the equation: one procedure uses iteratively the Gold-algorithm with a minimization of the χ^2-function [150]. Alternatively an approach invoking the Bayes-theorem is applied [117], where for each mass-energy-bin the probabilities have to be calculated for how the $\boldsymbol{y} = (N_e, N_\mu^{tr})$-cells will be populated. An iterative procedure tries subsequently to reproduce the given two-dimensional size-distribution of the data. Whereas the kernel function for the first approach is calculated by combining simulations of high statistical accuracy, using the thinning sampling method in order to reduce computing time [81] as well as full simulations to describe all physical and experimental effects (fluctuations of shower sizes, efficiencies, reconstruction accuracies), the latter approach requires a larger statistical accuracy of the simulations, but does not require the parameterization of response distributions.

In a first step the unfolding method based on the Gold-algorithm was applied to the one-dimensional spectra of the sizes, only. These were results of a preliminary nature reported by the KASCADE collaboration at the 27th International Cosmic Ray Conference 2001 [138,149], but they confirm the feature that the knee originates from the spectrum of light primaries (figures 35 and 36). Though the absolute fluxes and slopes of the different mass groups still show large

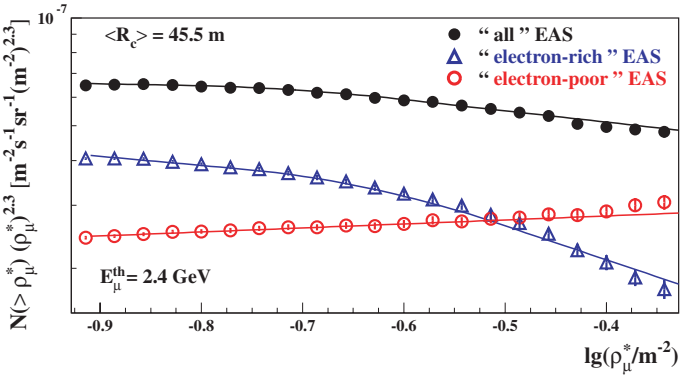

Figure 34. Spectra of the local muon density $\rho_\mu^\star$ ($E_\mu^{th} = 2.4$ GeV) for a fixed distance from the shower centre R_c for different EAS subsamples as measured by the KASCADE experiment (from [147]). Only light induced showers (electron-rich) show a knee in the corresponding energy range of 1–10 PeV.

uncertainties arising from the limited number of MC simulations, from model dependence and from methodological uncertainties, the results exhibit a rigidity dependent knee position. Results of the alternative non-parametric procedure [117] are also given in figure 36 which displays the mean logarithmic mass obtained by the unfolding procedures used in KASCADE. We would like to emphasize that non-parametric procedures indicate the methodical approach of a consistent data analysis on an event-by-event basis with minimum bias and with the potential to explore and to quantify particular sensitivities and uncertainties, e.g. arising from different answers from the models. Nevertheless there is still a number of systematic influences which need clarification before publishing a final result, though there is no doubt about the general trend: the mass composition gets heavier at energies above the knee observed in the all-particle spectrum, and the knee originates from the vanishing light component. This feature raises the question: where is the knee position of the heavy component?

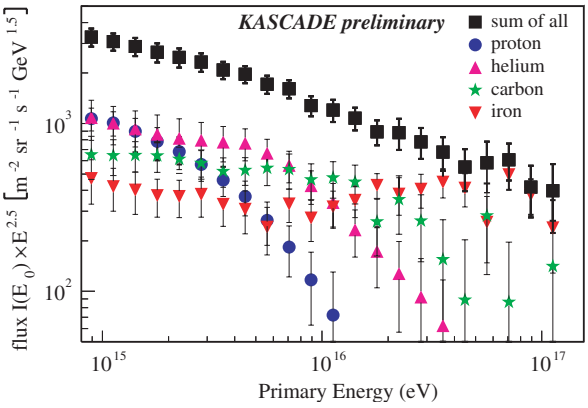

Figure 35. Energy spectra of four primary mass groups as obtained from an unfolding procedure applied to the KASCADE size spectra (from [149]).

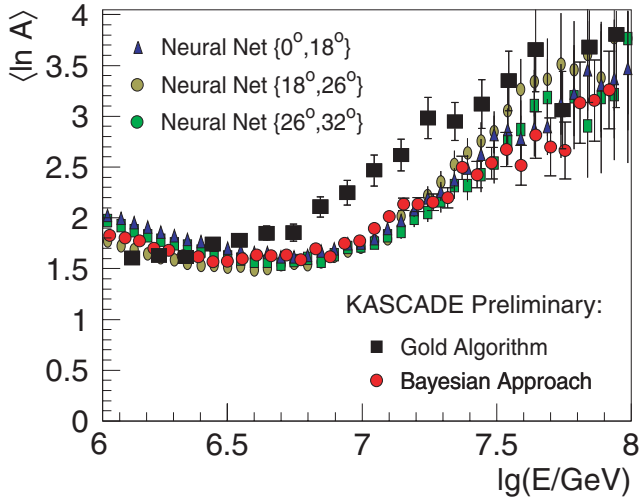

Figure 36. Mean logarithmic mass as obtained from unfolding procedures and a neural network applied to the KASCADE size spectra (from [117, 138, 151]).

4.4. Arrival directions

In the energy region where the interstellar magnetic fields scramble the propagation paths of charged primary cosmic rays, anisotropies in the arrival directions are extremely small, ever detectable, and difficult to determine. In fact so far no definite anisotropy has been found for energies around the knee. Nevertheless anisotropies of different mass groups would be interesting information for understanding the CR propagation in the galaxy [152].

5. Energy spectrum and mass composition of ultra-high-energy cosmic rays

In the range of the highest energies the first remarkable feature, in fact finally resolving an enigma, arises from the existence of radiation fields in the cosmos, of which the 2.7 K microwave background is the best known, filling the entire universe with radio to far-infrared photons with a density of ca $400\,\mathrm{cm}^{-3}$. Cosmic ray particles coming from long distances, inelastically interact with those background photons above some energy thresholds. High-energy incident protons for which the background appears to be blue-shifted, start photo-pion production (via exciting the $\Delta(1232)$-resonance in pions, and with less significance also by pair production $p + \gamma_{2.7\,\mathrm{K}} \rightarrow p + \mathrm{e}^+ + \mathrm{e}^-$) above a few tens of EeV and get quickly cooled down in this way. This is the predicted GZK spectral cut-off [5, 6]. The consequence is that above $\approx 6 \times 10^{19}$ eV, photons, protons and nuclei have rather short attenuation lengths, as a consequence of different processes during propagation, of the order of several tens of Mpc, and the universe gets relatively opaque for them. Stated more explicitly it appears impossible for ultra-high-energy cosmic particles to reach us from sources whose distances would exceed ca 100 Mpc [153] (this is roughly the size of our cosmic backyard, i.e. the local super-cluster of galaxies), unless rather exotic particles or exotic interaction mechanisms are envisaged. A second feature is related to the chemical composition of ultra-high-energy primary cosmic rays. If the highest energy cosmic rays were mainly protons, as some experimental results are tentatively interpreted, the trajectories of single charged ultra-high-energy particles through the galactic and extra-galactic magnetic fields (which are believed to be of the order of μG and nG, respectively) would get no more noticeably deflected over distances limited by the GZK cut-off. Typically the angular deviation of a 10^{20} eV proton from a source of 30 Mpc distance would be about 2°. In other words, above the cut-off, the direction of incidence of such particles (protons) should roughly point to the source, and to some extent proton astronomy should become possible, defined within the box due to consequences of the cut-off. However, looking in our astrophysical surroundings the number of adequate objects within a distance of a few Mpc and within the range of 2° from arrival directions of registered ultra-high-energy events is quite limited, if such objects were even able to accelerate particles to such extremely high energies at all. The question whether protons are indeed accelerated in BL Lacs to energies above 10^{19} eV is currently under debate (see [154, 155]).

The data around the ankle and above, stem from a few large-aperture ground based detector installations of two types of observation techniques, which are surface detector arrays for sampling the secondary charged EAS particles on ground and air fluorescence detectors viewing light tracks in the atmosphere. They are compiled in table 2.

UHECR[2] research started with the smaller Volcano Ranch array nearly 40 years ago. There the first air shower event with the symbolic limit of 10^{20} eV was observed [156]. Later on it was joined by the Sydney SUGAR array [157]. These detector arrays are included in

[2] For cosmic rays with energies above the predicted cut-off the term extremely high energy cosmic rays (EHECR) is often used.

Table 2. UHECR detectors (with number of events above 10^{20} eV taken from a compilation 2001 [164]). A recent restriction to events with zenith distance below 45° decreased the number of events seen by AGASA from 17 to 11 (private communication of Teshima, January 2003).

Array	Area (km^2)	Exposure (10^{16} m^2 sr s)	Detectors	N ($E > 10^{20}$ eV)
Volcano Ranch [156]	8	0.2	Scint.	1
SUGAR [157]	60		Muon	0
Haverah Park [158]	11	0.9	Water-Cher.	0
Yakutsk [159]	10	1.4	Scint., Air-Cher.	1
AGASA [160, 161]	100	6.0 (5.1)	Scint., Muon	17 (11)
Fly's Eye [45]		2.6	Air fluorescence	1
HiRes(I + II) [162, 163]		6.0	Air fluorescence	2

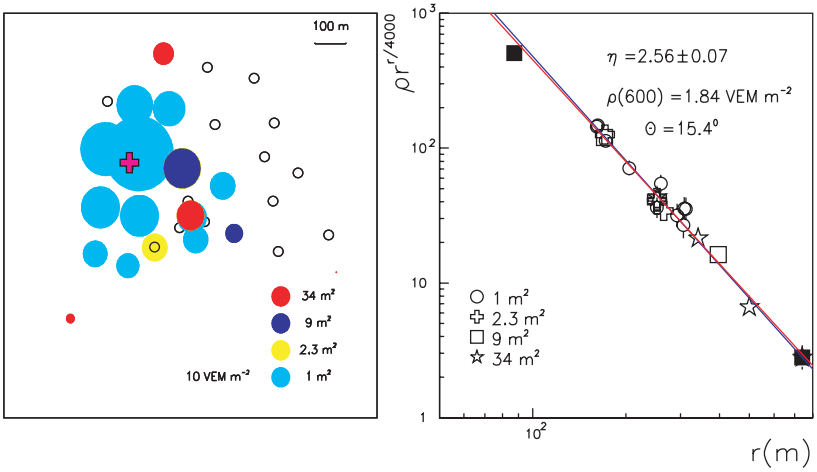

Figure 37. Example of the reconstruction of a high-energy event at Haverah Park. The radius of the circles in the left panel is proportional to the logarithm of the density in units of vertical equivalent muons (VEM). The right panel shows the lateral distribution of this event (from [165]).

table 2 just for historical reasons, though the accuracy of the SUGAR array, in particular, for searching extremely high-energy events has been rather poor.

The Haverah Park experiment in the UK [41] was an array of water Cherenkov detectors, operated by the University of Leeds and other UK groups. The data collected from 1968 to 1987 are still the basis of valuable analyses of EAS above energies of 6×10^{16} eV. In context with the Haverah Park experiment, the method of using the signal density produced by charged particles in the water Cherenkov detectors, registered at a distance of 600 m from the EAS axis, has been developed for the determination of the primary energy [81]. Due to reduced fluctuations of the density of particles (preferentially muons) at larger distances and, as simulations show, due to the insensitivity to the primary mass and the specific interaction model, this parameter $\rho(600)$ with the understanding $E = k \cdot \rho(600)^{\alpha}$ (α close to 1) has been proven to be a very robust energy estimator. Figure 37 shows an example of a measured density distribution of a high-energy cosmic ray event observed with the Haverah Park array. It displays the lateral density distribution which is described by the parameter η (see section 2.2.1).

The technique has been essentially adopted by the Yakutsk array [43, 159] and the AGASA experiment [160, 161]. The Yakutsk array in Russia is additionally equipped with 50 Cherenkov detectors for studying the Cherenkov light emission and checking the $S(600)$ method for the

determination of the primary EAS energy. The quantity $S(600)$ is the average energy deposit of the EAS particles in the scintillation detectors at $r = 600$ m, given in units of the energy loss of a vertically penetrating muon. In context with a global analysis of data from the Yakutsk array the question of the energy determination by $S(600)$ has been recently scrutinized on the basis of QGSJET MC simulations [166]. Yakutsk claims the observation of a giant EAS with a primary energy of 3×10^{20} eV [167]. However, there are difficulties in estimating the exposure and energy resolution so that these data are usually not included in the flux estimation. The AGASA experiment located in the Akeno observatory in Japan covers an area of 100 km^2 and is presently the world's largest detector array in operation. For the energy calibration via $S(600)$ the AGASA studies take into account the attenuation of $S(600)$ for inclined showers which pass through a larger atmospheric thickness [161].

The Fly's Eye [44] in Dugway, Utah, USA, was the first successful air fluorescence detector and demonstrated the power of the technique on primary energy and mass determination. Fly's Eye measured the highest-energy shower ever in 1991, with a reconstructed primary energy of above 3×10^{20} eV [8]. The HiRes Fly's Eye detectors [168] collect for each pixel of the fluorescence detectors the pulse height and arrival time, from which the EAS geometry can be reconstructed. It consists of two detector installations located in a distance of 12.6 km separated from each other. An important feature of the HiRes-I and HiRes-II [101] detectors is that showers viewed by both detectors (stereo events) can be measured with significant redundancy.

5.1. Structure of the spectrum: cut-off or not?

Recently [158] the data of the Haverah Park array have been reanalysed on the basis of improved MC simulations, with significant changes to previously published results (see [169]). The reanalysed energy spectrum between 1 and 10 EeV is displayed in figure 38. A remarkable feature is a dip indicated around 3×10^{18} eV with a change of the spectral slope [45]. The ankle appears clearly below 10 EeV, in contrast to the results of the AGASA collaboration. In fact, when comparing the results on the position of the ankle the five relevant experiments (Haverah Park, Fly's Eye, HiRes, AGASA and Yakutsk) show a disagreement in the range of 1–20 EeV (see figure 39 and the comparison in [170]).

Figure 40 displays the highest energy region of the cosmic ray spectrum as observed by the AGASA detector [171, 172]. The digits near the data points indicate the number of events and the bars show the 90% confidence level. The energy spectrum is multiplied by E^3, so that the lower part becomes flat. The ankle structure becomes evident with a deviation from the cut-off predictions, i.e. with an excess of ultra-high-energy events as compared with the spectrum expected from distant sources. The theoretical curve, which anticipates the GZK cut-off mechanism and an adopted distribution of the sources, indicates that the expected GZK cut-off is not an abrupt drop down, rather a suppression of the ultra-high-energy flux. Near the GZK cut-off energy an enhancement should also be expected due to a pileup effect of cosmic particles starting with higher energies and crowding up at energies just below the cut-off. There are of course large error bars, but the tendency of the existence of a trans-GZK cosmic flux could be considered to be established when other events are included from other detectors (see the review of Nagano and Watson [2]). In the past also Fly's Eye and the HiRes collaboration have reported a number of trans-GZK cut-off events (see, e.g. [45, 9]).

Thus, though the experimental basis was still poor and under debate, till 2001 there seemed to be a, maybe somewhat biased, but tacit common understanding on the fact that the ultra-high-energy cosmic ray spectrum extends to energies $> 10^{20}$ eV. However, after a re-calibration by the HiRes collaboration with withdrawing some results, a discussion during the last International Cosmic Ray Conference in Hamburg 2001 made it obvious that there is a disagreement of

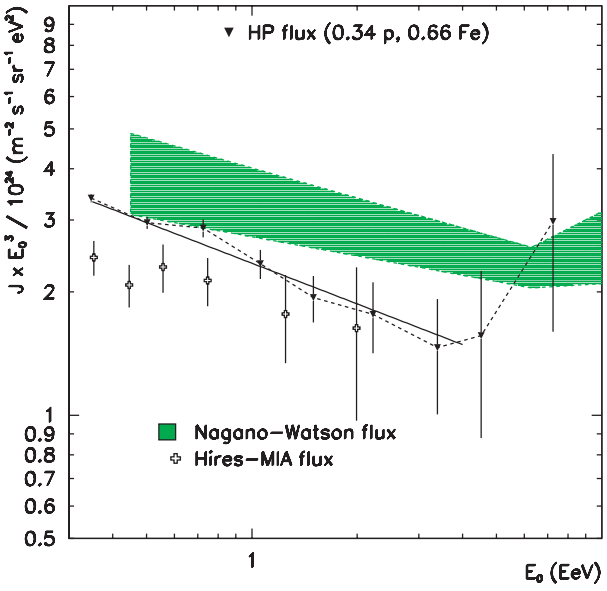

Figure 38. Energy spectrum obtained from Haverah Park data assuming a bi-modal composition of 34% proton and 66% iron. The lines show a fit to the spectrum obtained and are compared to other results (from [158]), including the flux estimated by a combination of data from HiRes fluorescence and the MIA muon detection devices.

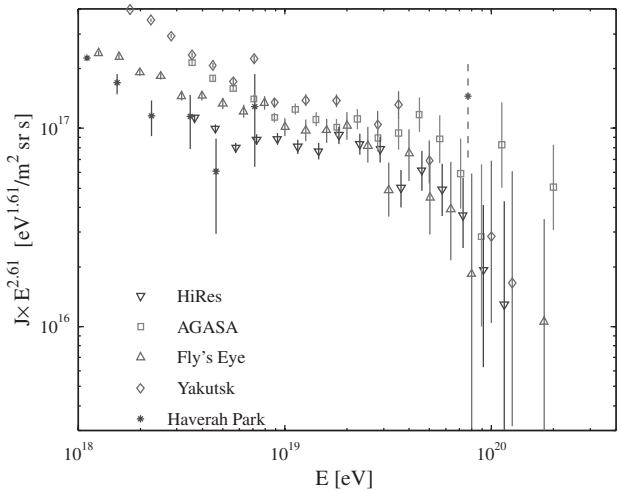

Figure 39. Energy spectra above 10^{18} eV obtained from various experiments (from [158], HiRes [162], Agasa [7], Fly's Eye [45], Haverah Park [158]).

different observations, between the AGASA and HiRes results in particular, concerning the inferred fluxes and the energy calibration. Though this disagreement has been subsequently somehow relieved by a serious revision of the previously reported events, it is not definitively removed. In recent papers of the HiRes [162, 163] and AGASA collaborations [173] this situation is discussed.

Figure 41 compiles recent results, comparing the monocular spectra from both the HiRes-I and HiRes-II detectors with the latest results of the AGASA experiment. The highest energy

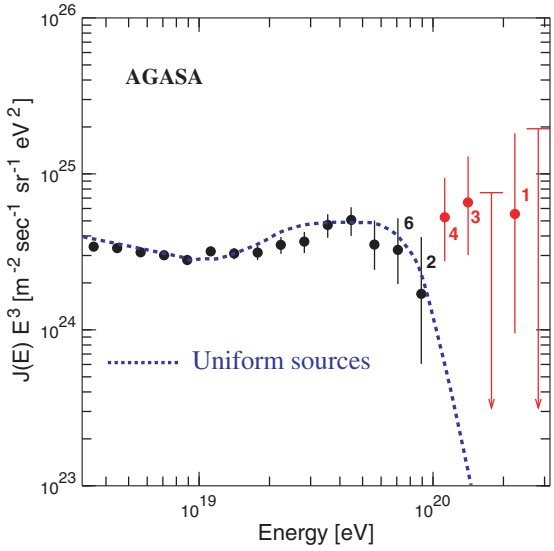

Figure 40. Highest energy region of the cosmic ray spectrum [172] from AGASA (1999).

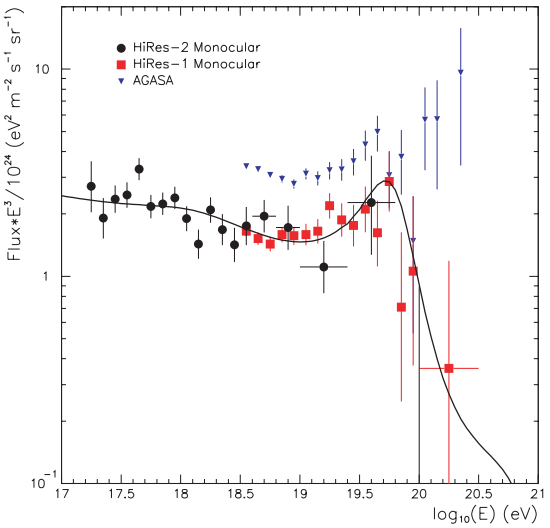

Figure 41. Comparison of the results of HiRes and AGASA on the ultra-high-energy cosmic ray flux. The HiRes results which appear to be consistent with the GZK cut-off have been analysed in terms of a model with uniformly distributed proton sources [163]. The revised data of AGASA still clearly show events above the expected cut-off (see text).

event observed with HiRes is at the reconstructed energy of 1.84×10^{20} eV. The AGASA results, most recently updated [174], have excluded events with zenith angles larger than 45°, and they differ from the communication at the 27th ICRC in Hamburg 2001 [161]. Obviously, below 10^{20} eV the AGASA flux consistently differs from the HiRes observations, which appear to be pronounced in the $J(E) \cdot E^3$ presentation in the figure. In fact a 20% lowering of the energy scale of the AGASA experiment would reduce this disagreement considerably. The HiRes spectrum appears consistent with existence of the GZK cut-off. The line represents a fit

assuming the GZK cut-off mechanisms for particles accelerated by galactic and extragalactic sources, uniformly distributed across the universe [175]. Above 10^{20} eV the HiRes spectrum, as it stands, and also the reanalysed spectrum communicated by the Yakutsk experiment [176], significantly differ from that reported by the AGASA experiment. A recent discussion of this observational situation, with the question 'Has the GZK cut-off been discovered?' is given by Bahcall and Waxman [170]. The results from different experiments are compared, with small adjustments in the absolute energy scale (within the quoted systematic uncertainties), and all measured fluxes can be brought in agreement at energies below 10^{20} eV. Only the reported AGASA flux above 10^{20} eV is higher than that measured by HiRes, which seems to be consistent with the existence of the GZK cut-off. Thus we may conclude that the existing data still leave the question open.

5.2. Elemental composition

Figure 42 compiles the recent experimental information about the variation of the mass composition of the ultra-high-energy cosmic rays as mapped by the variation of $X_{\max}$. The information is carried by the position of the shower maximum $X_{\max}$, which can be determined either from the reconstruction of the longitudinal EAS development by the air fluorescence technique or from the slope of lateral distribution of the Cherenkov light.

The mass discrimination effect arises from the fact that protons penetrate deeper into the atmosphere than expected for heavy nuclei of the same energy. Thus a change in the elongation rate, beyond the change for an individual element, will indicate a change in the mass composition. However, a calibration is needed by referring to a hadronic interaction

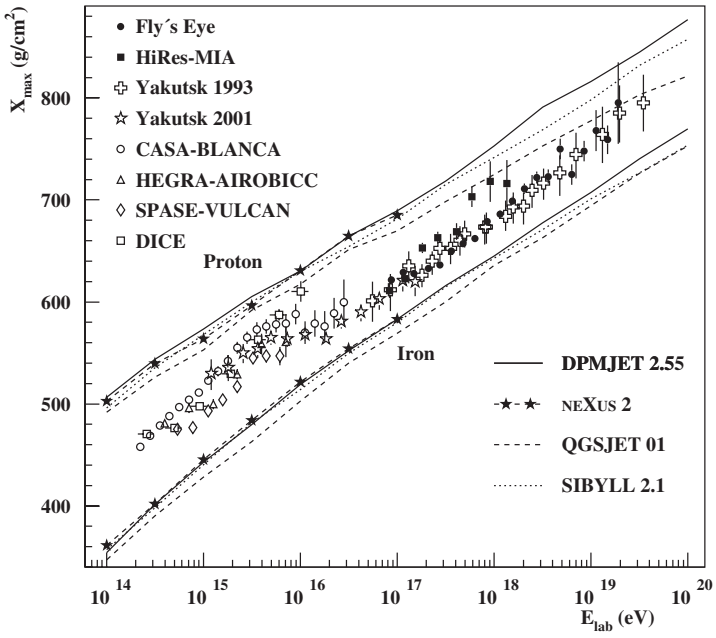

Figure 42. Average depth $X_{\max}$ of the EAS maximum vs the primary energy from various measurements [108, 177]. The experimental results are compared to predictions of four different hadronic interaction models for proton (upper curves) and iron (lower curves) primaries (Fly's Eye [45], Hires-Mia [178], Yakutsk93 [179], Yakutsk01 [176], BLANCA [22], HEGRA [24], SPASE [48], DICE [142]).

model for the MC simulations. Several theoretical curves in figure 42 display the model differences. They include also the predictions by a rather new event generator NEXUS of great universality [180]. Qualitatively, the mass composition appears to be mixed or heavy just above the knee with a global trend, starting around a few 10^{17} eV, towards a light composition in the energy range around 30 EeV [181]. Initially the studies of the AGASA data by Hayashida *et al* [182], basically exploiting the (N_e, N_μ)-correlation, came to the conclusion that the chemical composition does not change at higher energies. A critical reanalysis, however [183], clarified inconsistencies by differences in the invoked hadronic models and reconciled the Akeno results with the X_{max} observations. This is a further example of the limitations due to the deficiencies in our knowledge of hadronic interactions at high energies. In the context of the debate about the possible origin of ultra-high-energy cosmic rays experimental information about the fraction of photons in primary cosmic rays is of importance. Constraints are derived from Haverah Park data [184] and from the analysis of the EAS muon component observed by AGASA [185], the latter permitting a contribution of gamma ray primaries with an upper limit of 28% (at 90% confidence level) for energies above 10^{19} eV.

5.3. Arrival directions

In 1999 Hayashida *et al* [186] reported a directional anisotropy for EAS events in the energy range of (1–3) $\times$ 10^{18} eV, which provides evidence that EeV cosmic rays have sources in our galaxy (figure 43). This finding, which is on a few per cent level in the size of the anisotropy, is corroborated by observations of Fly's Eye [187]. In contrast above 10^{19} eV cosmic rays display apparent isotropy [172], though some event clusters may be identified with low chance probability. As far as such conclusions can be drawn with this statistical significance, the distribution of the arrival directions does not exhibit a significant galactic-plane enhancement. This feature, together with the trend to a light mass composition, supports the assumption that an extragalactic cosmic ray component comes into play at the highest energies.

This observational situation is characterized by many experimental uncertainties, and the discussion is dominated by the quest for a higher statistical and systematic accuracy to prove or to disprove the actual, more or less bold, conjectures. It implies consequently a call for new, powerful experimental installations (see section 8).

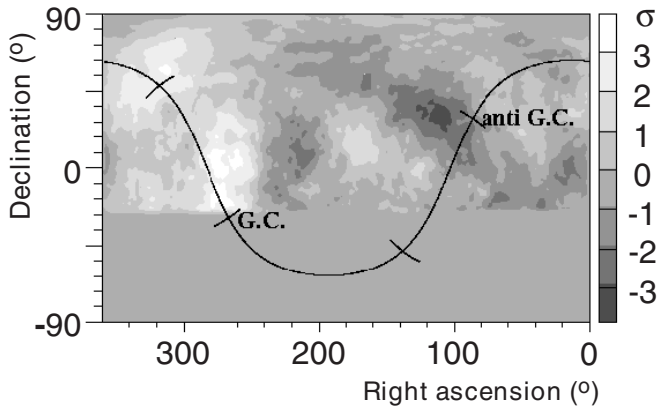

Figure 43. Significance map of anisotropy for EAS events between 8 $\times$ 10^{17} and 2 $\times$ 10^{18} eV in equatorial coordinates observed by AGASA [186]. Direction of galactic centre (GC) and anticentre (anti-GC) are shown. Events within a radius of 20° are summed up in each bin.

6. Comments on high-energy interaction models

Microscopic hadronic interaction models used as generators of EAS MC simulations by programs like CORSIKA [15], AIRES [106] or MOCCA [81], e.g., are based on parton–parton interactions and approaches, inspired by QCD, considering the lowest-order interaction graphs involving the elementary constituents of hadrons (quarks and gluons). However, there are not yet exact ways to calculate the bulk of soft processes, since for small momentum transfer the coupling constant α_s of the strong interaction is so large that perturbative QCD fails. Thus we have to rely on phenomenological models which incorporate concepts of scattering theory. A class of successful models is based on the Gribov–Regge theory [188]. The momenta of the participating partons are generated according to phenomenologically motivated distributions and measured structure functions. Models like SIBYLL [189, 190], QGSJET [191], VENUS [192], DPMJET [193] (and others and in different updated versions), which are specifically used as generators of advanced EAS MC simulations, describe particle production by exchange of one or multiple Pomerons. Inelastic reactions are simulated by cutting Pomerons, finally producing two colour strings per Pomeron which subsequently fragment into colour neutral hadrons. Differences between the models arise from the particular implementation of the Pomeron concept and string fragmentation. An important difference is that QGSJET, SIBYLL and DPMJET are able to treat hard processes (which can be calculated by perturbative QCD), whereas VENUS does not do so. VENUS and DPMJET on the other hand allow for secondary interactions of strings which are close to each other in space and time. A qualitatively new ansatz was made with the NEXUS model [180] where the Gribov–Regge theory was applied directly to partons, including full energy momentum conservation at amplitude level. Due to the phenomenological character of the models data are needed to tune the free parameters and to verify or to falsify theoretical assumptions of the models. In particular, the model predictions depend sensitively on the low-x extrapolation of the parton densities.

Realizing that presently available collider data end at some 10^{15} eV (equivalent laboratory energy of the Tevatron collider) and that such models have to be extended to ultra-high-energies over several decades, it is a question of urgent interest, how the theoretical developments can be guided and controlled by experimental findings. Thereby one has to emphasize that the efforts have to be predominantly focused to the forward, i.e. diffraction region with low momentum transfer of the hadronic collisions, since this part of the kinematical range drives the air showers. With this view the schedules and experimental plans of forthcoming accelerator experiments have been recently discussed in a workshop organized in Forschungszentrum Karlsruhe: NEEDS from Accelerator Experiments for Understanding High-Energy Extensive Air Showers, developing a list of desired information from accelerator experiments that could be used for constructing more accurate and realistic hadronic interaction models [194–196]. Here, a co-operation between present and future accelerator experiments and cosmic ray investigations is aspired to. Physicists of both the high-energy accelerator and the cosmic ray communities, together discussed future possibilities of mutual assistance and exchange of data of relevance to model construction. This necessity has been further stressed and specified by a subsequent NEEDS workshop at the 12th ISVHECRI, 2002 (see Schatz [197]).

However, cosmic ray physics may also directly contribute to a better understanding of the high-energy hadronic interaction in the forward region by specific investigations:

(i) Testing hadronic interaction models by EAS data. Various (preferentially hadronic) observables as predicted by the MC simulations within the uncertainty of the primary elemental spectrum can be compared with the measurements, thus shrinking the range of realistic models and pointing out obviously inconsistent model features [89, 90]. The advantage of a multi-detector experiment like KASCADE measuring simultaneously many

EAS observables, is obvious. By applying a suitable discrimination method the (N_e, N_μ)-correlation could be used to prepare event samples, which get highly enriched by EAS events induced by a defined mass group. For such enriched samples [91], other relevant observed EAS parameters could be studied and compared with simulations without the need of an *a priori* assumption of a primary mass composition. The non-parametric procedures and applications (e.g. outlined in [122]) are of special interest.

(ii) Attenuation length and longitudinal development. There are various EAS quantities which can be nearly directly related to ingredients of hadronic interaction models, like the so-called attenuation length Λ to the inelastic cross-section $\sigma^{\text{inel}}_{\text{p-air}}$, deduced, e.g., from observations of the size spectra, registered with different angles of EAS incidence, i.e. with different atmospheric target thickness (see the approaches in [198–202] and for a critical discussion of the subject see [203]). In addition the longitudinal EAS development, which may be studied with optical detectors, is not only driven by the inelastic cross-section of the primary particle, but also on cross-sections of the secondary particles (pion–air cross-sections) and the inelasticity K of the hadron–air interactions. K is the fraction of energy that is carried away by the secondary particles produced (see, e.g. [107]).

(iii) Calorimetric measurements at high-mountain altitudes. The feature that the most energetic particles in initial EAS stages are concentrated in the shower core is the basis of the traditional EC experiments at high-mountain altitudes on Mt Chacaltaya or on the Pamir plateau [55]. As already indicated in section 2.2.5 the potential of calorimetric devices installed at high-mountain altitudes for studying hadronic interactions in energy ranges, where collider experiments do not necessarily give the required answers, is rather promising. Nevertheless it is our feeling that the EC technique has to be modernized towards the use of active detectors at high altitudes with a fast signal processing and event-visualization. In addition such calorimeters should be embedded in a multi-detector array enabling adequate triggers and complete specifications of the observed events. Ideas in this direction and future prospects have been discussed in more detail by Saavedra [204] for the case of Chacaltaya.

7. Astrophysical implications of the present knowledge

7.1. The knee region

For the origin of cosmic rays observed in the energy regime around the knee between 1 and 10 PeV various models are under discussion. Supernova remnants have been recognized [205], up to several PeV, as plausible sites for Fermi shock acceleration processes. Massive supernova progenitors may accelerate even up to higher energies [206] (see also the review [207]). Though there is direct evidence for electron acceleration in x-rays and TeV gamma rays, the evidence for hadron acceleration is still missing, suggesting that the energy cut-off may be below the knee energy. Thus the origin of cosmic rays of the knee region is still a puzzle, and the present knowledge about the variation of the mass composition may exclude some possibilities, but it remains too uncertain for a discrimination of the different models. Figure 44 displays the predictions of four different models which explain the origin of the knee on the basis of the rigidity dependence of acceleration and propagation of cosmic rays. The variation of the mean logarithmic mass in comparison with recent results from KASCADE is shown. The experimental variation results from different data analyses of various degrees of sophistication, and the differences reflect essentially methodical uncertainties of the present state-of-the-art. It should be noted that due to the obvious necessity to clarify methodical influences, KASCADE

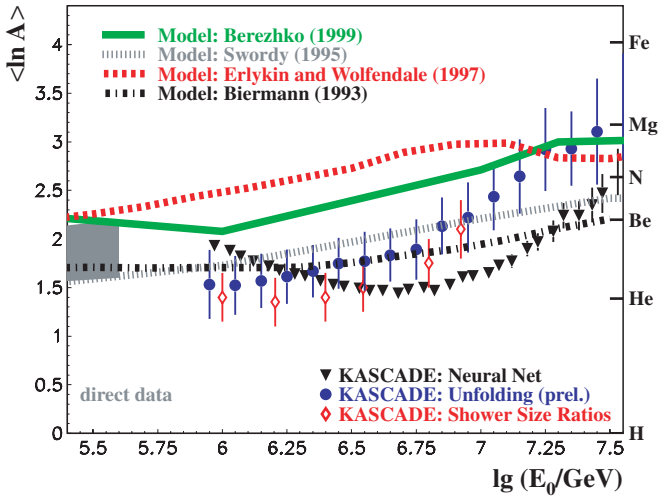

Figure 44. The mean logarithmic mass distributions resulting from different analyses of the KASCADE experiment [122, 138, 110]) as compared with predictions of astrophysical models for the origin of the knee (Berezhko [126], Swordy [208], Erlykin and Wolfendale [71], Biermann [127]).

has not yet published a final result. It is evident that the uncertainties of the EAS experiments are presently of the same order as the differences of the astrophysical model predictions. Nevertheless the experimental results favour a relatively light mean logarithmic mass of the cosmic ray elemental composition below the knee. This is obviously in disagreement with some models, in particular with the single source model of Erlykin and Wolfendale [71] where the knee is mainly due to a composition dominated by oxygen nuclei, with a steeply falling proton component below the knee, leading to a large mean mass number. Models with a simple rigidity dependent knee and identical slopes below and above the knee (e.g. the Biermann-model [127]) agree tentatively better with the data. More definite conclusions, however, are presently hardly possible.

Even if the knee could be explained by rigidity dependence, the question remains open, whether this is due to the source spectrum, i.e. due to a cut-off of the acceleration process in our galaxy or by the charge dependent escape of the particles from the galactic magnetic field. The considerations of Swordy [208] take both effects into account. For discrimination additional information is necessary, e.g. anisotropy measurements for single mass groups in the energy region above the knee.

7.2. Above the ankle

The existence of UHECR events constitutes an enigma: where are the sites and what are the acceleration mechanisms capable of imparting energies of macroscopic orders to a microscopic particle? Many processes have been proposed [209] where in an astrophysical plasma large-scale macroscopic motion is transferred to individual particles, for example, in turbulence and by shock waves. The crucial role is played by the size L of the acceleration region and the magnetic field B embedded in the plasma and keeping the gyro-radius of the particle in the acceleration region. The gyro-radius depends also on the velocity β of the motion (in the conventional approach of shock wave acceleration by the Fermi mechanism, say in supernova remnants, β is in the order of 0.01).

Traditionally astrophysical accelerator candidate sites are compiled by a (B vs L)-plot introduced in 1984 by Hillas (figure 45), often adopted with various modifications. It is constructed for an estimate of the maximum total energy $E_{\max} \propto \beta \cdot Ze \cdot B \cdot L$ of the particles, neglecting energy losses from synchrotron radiation or the interaction with the microwave background. This dimensional constraint already rules out most astronomical objects. Possible objects include radio galaxies, neutron stars and active galactic nuclei. Additionally gamma ray bursts as sources of zevatrons (1 ZeV $= 10^{21}$ eV) have been discussed ([211], see also [212]). If all parameters related to the question are taken into account, one has to concede that none of the proposed scenarios is fully convincing. In addition we have to keep in mind that the sources should be near by on cosmological scales. Within statistical accuracy the data also do not show a distinct correlation with nearby point sources. There are various examinations of the arrival directions of the highest energy events. Ahn *et al* [212] proposed a galactic wind model for the local magnetic fields and traced back trans-GZK cut-off events within 20° from the active galaxy M87 in the Virgo cluster (about 20 Mpc away). They had to assume that the two cosmic particles registered with the highest energies (2×10^{20} and 3.2×10^{20} eV) are He particles. In fact, there is a suggestion for the origin of trans-GZK cut-off events that they are produced by heavy nuclei, since the energy loss times for heavy ions of energies $>3 \times 10^{20}$ eV are longer than for protons [213]. In the case that the hypothesis of a galactic wind accelerator turned out to be real, proven by larger statistical accuracy of the observations, a gigantic accelerator would have been discovered, reaching energies many orders of magnitude higher than any conceivable man-made machine.

However, if future studies were to exclude conventional astrophysical acceleration mechanisms, one would need to consider another class of theories proposed as possible explanations, so-called top-down processes. Most of those speculations study the possibility that UHECR arise from the decay of some super-heavy X particles whose mass is in the grand unification range (10^{25} eV) produced during a phase transition period or by topological defects during the early universe. The models differ mainly in how to produce the density of X particles to fit the UHECR observations and their survival from some 10^{-35} s after the Big Bang. An

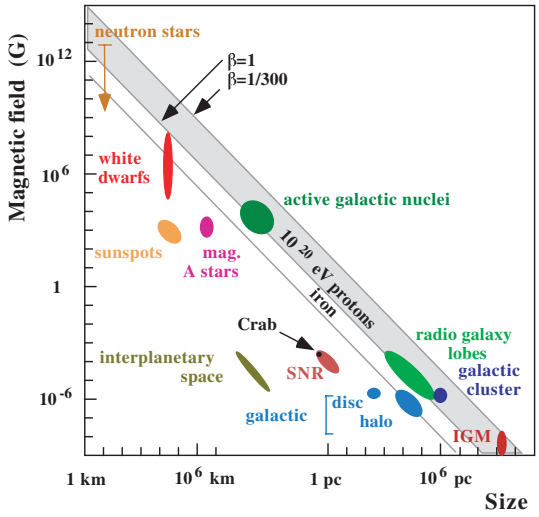

Figure 45. Possible UHECR acceleration sites plotted by their magnetic-field—size correlation (so-called Hillas-plot) [210].

extensive review about top-down models is published by Bhattacharjee and Sigl [214] with an exhaustive list of references. Great interest has been induced by the idea of Z-bursts, that extremely ultra-high-energy neutrinos ($\sim$10 ZeV) could produce ultra-high-energy Z-bosons by interactions with thermal background neutrinos (see, e.g. Fodor [215]). However, with such a conjecture the problem appears shifted to the question of a source of 10 ZeV neutrinos. It has been also suggested that at ultra-high-energies the neutrino nucleon cross-section would increase to hadronic values (100 mb), so that neutrinos could produce giant air showers [216]. Another unconventional idea, which has already been discussed in the 1970s [217–219], is that the Lorentz invariance might be weakly broken at ultra-high-energies so that photo-pion production and hence the GZK cut-off get suppressed.

One should mention that such speculative models and the numerous ideas *en vogue*, arising with the prospect of new physics and new astrophysics, have quite specific features and experimental signatures (shape of the spectrum and mass composition) so that discrimination appears not to be impossible, provided the experimental knowledge could be sufficiently increased. For example, the presence or absence of the pileup at the predicted GZK cut-off energy could be a signature for bottom-up or top-down models, respectively. Top-down scenarios should also produce a large ratio of ultra-high-energy photons to protons [220], which seems not to be consistent with the present muon content and $X_{\max}$ measurements.

8. Outlook to the next decade

8.1. Around the knee

Most of the present detector installations measure around the knee region or they are optimized for much higher energies around the GZK cut-off. Practically none of the modern multi-detector experiments is specifically dedicated for the energy range of 10^{16}–10^{18} eV. Only the Yakutsk array [137] which registers air-Cherenkov radiation from EAS covers the full energy range from the knee region to GZK cut-off energies. The interest of some newer EAS observation experiments is directed to studies of high-energy gamma ray sources in the TeV region probing in this way the origin of primary cosmic rays [221]. Such experiments measure as 'background' charged cosmic rays up to the knee region. There are several ideas to use this background for studies relevant for primary mass composition, but corresponding activities are so far not well elaborated. Nevertheless the data can be used to improve the results and/or to test the interaction models at moderate energies. Recent MC studies prove also the sensitivity of present and future telescopes needed to measure the direct Cherenkov light produced by the primary in the upper part of the atmosphere [222], which would lead to a very good mass resolution.

Recent investigations for long duration balloon flights equipped with transition radiation detectors of large sensitive area are expected to extend the direct measurements up to energies of 5×10^{14} eV. Such balloon projects like TRACER or CREAM are presently under development [223, 224]. Also satellite-borne experiments or installations on the international space station are proposed which will try to investigate direct measures of the high-energy cosmic ray particles (see, e.g. [225]). Direct measurements of cosmic rays in the knee region obviously need a further decade for realization.

For the consolidation of the rigidity dependent knee position (i.e. ascribing the knee to an astrophysical origin and excluding the possibility of an alteration of the interaction, which should scale with the atomic mass) a kink in the heavy (iron) component at $\approx 10^{17}$ eV must be definitely identified, proving previous indications [45] that 'there is a second knee somewhere between 10^{17} and 10^{18} eV' [226]. Such an experimental indication is necessary

in order to confirm the above stated results and to match the total energy spectrum at higher energies. Figure 46 shows that the extrapolation of the present results (ascribing the knee to the light component) exceeds the measured all-particle spectrum in the energy region above 10^{17} eV. In order to address this question, the KASCADE experiment is going to be extended (KASCADE-Grande [36]), covering an area of $600 \times 600\,\mathrm{m}^2$ by installing the scintillation detectors of the former EAS-TOP experiment at the site of the Forschungszentrum Karlsruhe. The KASCADE-Grande experiment will include the full information provided by the original KASCADE multi-detector set-up for each measured single event (figure 47). The extended detector installation will be able to measure the CR energy spectrum and mass composition up to 10^{18} eV. The multi-parameter set-up will also enable consistency studies of the high-energy hadronic interaction models. This possibility is of great importance as a step towards the development and tests of the high-energy hadronic interaction models (see Ostapchenko [228]) used for interpreting ultra-high-energy cosmic ray observations.

Thus focal points of the cosmic ray research in the knee region and above are:

- The detailed shape of the energy spectrum, and spectra of single mass groups. Is there a smooth or a sharp change of the spectral index? Do fine structures exist? What is the variation of the elemental composition or of the knee positions of the different elemental components with the energy? Do the knee positions scale with charge or mass number?
- Test of astrophysical models of cosmic ray sources and acceleration mechanisms.
- Investigations of hadronic interactions in the *terra incognita* $E > 10^{15}$ eV and reducing the model dependence.

We characterize the present status by the obvious dilemma, that the elaborated analyses of the measured data are limited by a distinct dependence of the results on the adopted high-energy interaction model. Though, in contrast to other current experiments, the KASCADE-Grande experiment is able to specify the inherent model dependence, thanks to the large number of observables studied simultaneously in an event-by-event mode, any substantial progress needs an improved knowledge of the interaction models.

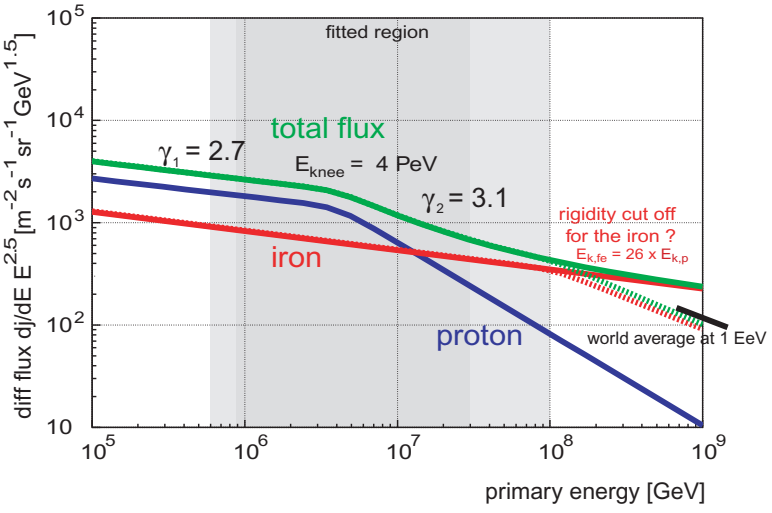

Figure 46. Motivation for the KASCADE-Grande experiment: Is there also a knee at the spectrum of the EAS induced by heavy primaries (from [36])?

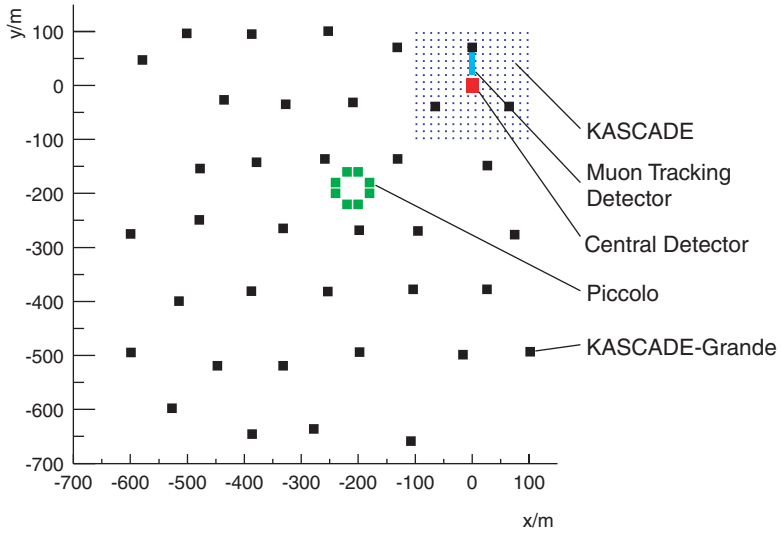

Figure 47. Layout of KASCADE-Grande, including the original KASCADE array (with all facilities) and a new trigger array Piccolo [227].

8.2. Ultrahigh-energy cosmic rays

The AGASA ground based array and the HiRes fluorescence detectors are continuing to collect data on ultra-high-energy EAS. The Japanese Telescope Array has been planned to be operated as an array of several telescopes for gamma ray and UHE neutrinos, but also for UHECR observations [229]. However, the future of this project is unclear. The community looks forward with great interest to the next detector. The PAO [12] with 14 000 km^2 sr aperture over two sites, one in each hemisphere. The southern hemisphere is of special interest, since here the centre of the galaxy is visible.

The installation of the southern PAO [12] started in 2000 with a prototype array of 55 km^2 and an air fluorescence telescope, near the small town of Malargüe in the province of Mendoza, Argentina. In the end the site will be equipped with 1600 detector stations (12 m^3 tanks filled with purified water detecting the Cherenkov light produced in the water tanks by secondary particles), distributed in a grid with 1.5 km spacing. The stations of the surface array will be operated by battery backed solar power and will communicate with the central station by wireless links. Four eyes composed altogether of 24 air fluorescence telescopes, will view 3000 km^2 of the site and measure during clear moonless nights, i.e. with a duty cycle of 10%, the giant showers through air fluorescence (figure 48).

The concept of a hybrid detector (figure 49) provides unique advantages. A subsample of 10% of the total number of events simultaneously observed with both techniques, enables a cross-calibration and a combined analysis, and yields an unprecedented quality of shower identification. It is expected to detect some 60–100 events per year above 10^{20} eV, and 100 times more above 10^{19} eV. Figure 50 displays an event as registered by the prototype fluorescence telescope in February 2002 [230]. This (hybrid) event has been simultaneously seen with the surface detector array.

The next observations with the fully installed PAO may clarify the question put by the present results: existence or non-existence of the GZK cut-off? In general the focal points of the forthcoming experiments may be summarized as

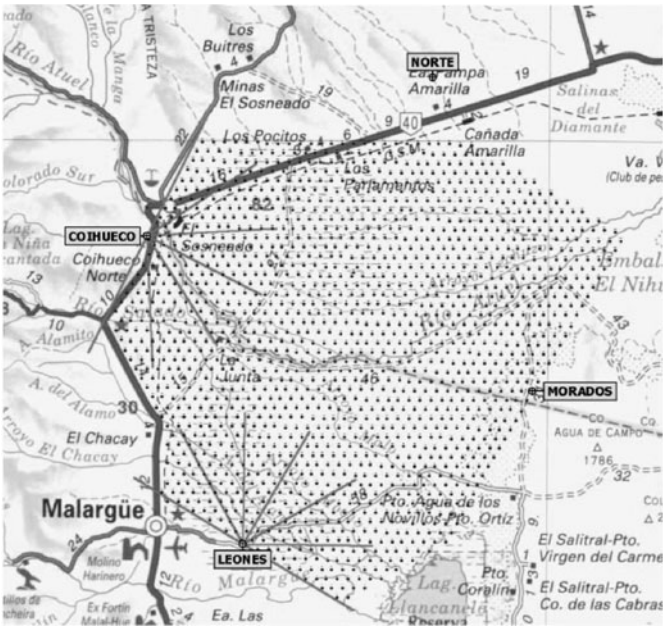

Figure 48. Layout of the southern PAO.

- The change of the spectral index at the ankle. Is there a change in the production mechanisms of UHECR? Is there a change in the elemental composition? Is there a change in the interaction processes?
- Shape and composition of the energy spectrum of the highest energies. What is the maximum cosmic ray energy? Is there any limit? Does evidence exist for a pileup bump at the end? Is there evidence of the existence or non-existence of the GZK cut-off? What is the mass of the primary particles of highest energies?
- Search for signatures of the origin of UHECR. Scale and coordinates of anisotropies or point sources? Is a bottom-up acceleration or is new physics of top-down processes responsible for the highest energies only few decades below the grand unification energy?

The PAO has just started with prototype observations, and the community already looks forward to beyond the next generation of detectors. There is little doubt that the next big step will be an air-borne detector observing the giant shower development in the atmosphere with a huge aperture down to the Earth's atmosphere.

This is envisaged to take place with the orbiting wide angle light (OWL) collectors Airwatch mission by fluorescence detectors carried on two satellites in a low Earth orbit (600–1200 km) and observing (in a stereoscopic mode) giant EAS from space [231, 232], also with the perspective to open the way for neutrino astronomy in the high-energy range. Operating from space dramatically increases the active volume and the observed EAS event rate. The OWL is expected to be able to detect more than 1000 EAS per year of energies above 10^{20} eV, provided the spectrum follows the trend of the AGASA results.

At present there is a feasibility study of the European Space Agency considering an extreme universe space observatory (EUSO) to install such a detector (figure 51) on the International Space Station and to develop the technology. Another proposal of this kind is a balloon borne project using the antarctic ice as reflector of Cherenkov light [49].

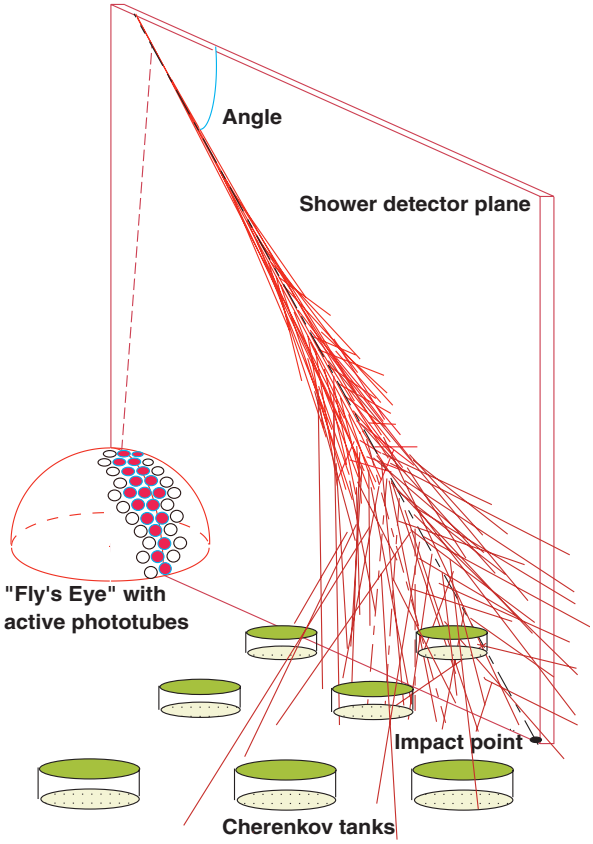

Figure 49. Hybrid detector concept.

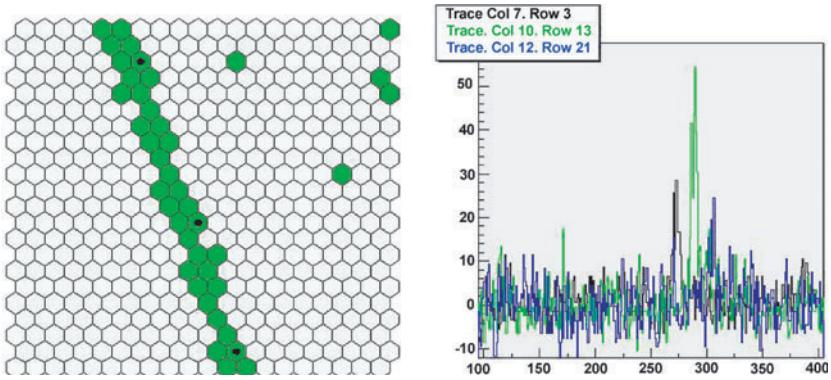

Figure 50. Display of an event registered with the prototype air fluorescence telescope. In addition to the trace in the camera the time variation of the amplitude is shown. The timescale is in ns [230].

The future projects are of particular interest since in a few years the spectrum may be shown to be exceeding the reach of the PAO, and larger statistical accuracies again would be necessary for studies of problems revealed by EHECR observations. In particular the high statistics are needed to examine anisotropy studies, studies of horizontal showers (most probably induced

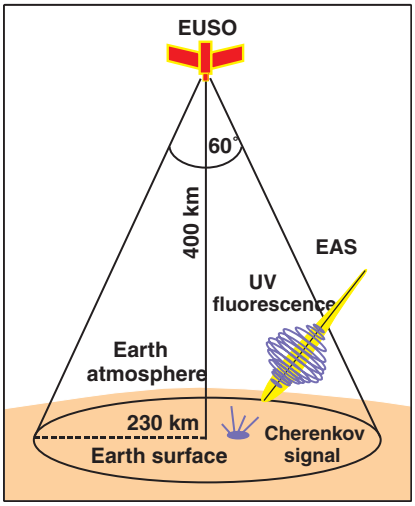

Figure 51. Principle of the EUSO detector [231].

by cosmic neutrinos) [233], and studies of the extragalactic magnetic fields via the features of the GZK cut-off [234].

9. Concluding remarks

Though there is considerable progress in detailing our experimental knowledge about the shape of the energy spectrum and on the mass composition of cosmic rays in the knee regime, no general agreement has been reached up to now. The results generally suffer from the fact that due to the low flux of cosmic rays above 1 PeV, only large ground based detector installations, observing EAS, can provide experimental data. However, the sensitivity of EAS observables to the mass of the primary cosmic rays is generally weak and clouded by considerable fluctuations of the EAS cascade processes in the atmosphere. In addition the analyses of the EAS data are subject to various uncertainties. The approach of the KASCADE experiment, in particular, observing correlations of a larger number of EAS observables attempts to overcome many systematic uncertainties. Nevertheless the present status is far from having completely removed such uncertainties. Rather, thanks to detailed methodical studies, it has revealed and quantified the inherent limitations and has specified further necessary improvements. While the present progress with promising results induces the hope that methodical difficulties will get clarified in near future, still there remains the model dependence of the results since any EAS analysis has to rely on *a priori* assumptions and reference patterns prepared by extensive MC simulations. Nevertheless the detailed investigations in the last decade make us quite sure that the knee at 3–5 PeV is caused by a decrease in the galactic flux of the light mass nuclei. It is not excluded that in future these results will be confirmed by direct balloon- and space-borne observations, which could be extended for light nuclei at least in the lower energy region near the knee.

The difficulties of interpreting the EAS observation will also accompany the studies of cosmic rays up to the highest energies. At the moment the most urgent clarification concerns the questions of the existence of the GZK cut-off and the flux of trans-GZK events. For that the community looks forward with great interest to the observations of the PAO. The theoretical speculations about the origin of trans-GZK events obviously go ahead of the definite experimental confirmation. A lesson of the advanced studies of the knee region like with

KASCADE is that investigations of far-reaching physical and astrophysical aspects by EAS observations have to be supported by a serious and quantitative understanding of the particle interactions in that energy range. That is a challenging task which cannot be disentangled from the astrophysical aspects. Without knowing the interactions of the unknown particles, even the energy estimation of giant EAS and the scale of the spectrum will remain finally under debate. It is fair to note that many analyses of UHECR EAS events and confusing results suffer from the use of less matured interaction models and that an impact, like that of the development of detailed shower simulation codes like CORSIKA for the research at the knee, is needed. The uncertainty in the hadronic interaction in the *terra incognita* may be also reduced in future by dedicated studies with present and forthcoming accelerators.

With such caveats in mind the prevailing understanding of the present situation of UHECR research may be characterized by the fact that investigations have not yet found a definite natural end of the energy spectrum. Anticipating the spectrum would extend beyond the GZK cut-off, there is a plethora of interesting speculations, but presently we are not able to identify experimentally or clearly specify signatures of the origin and cosmic sources of such a trans-GZK radiation. The features of this observation establish a real mystery of great cosmological relevance at the frontier of natural science.

Acknowledgments

We would like to thank Ralph Engel, Johannes Knapp and Hermann-Josef Mathes for clarifying discussions about the current status of the subject of this review, and to Masahiro Teshima for private communications. One of us (MR) gratefully acknowledges support from the Alexander von Humboldt Foundation and from the British Council.

References

[1] Kulikov G V and Khristiansen G B 1959 *Sov. Phys. JETP* **35**
[2] Nagano M and Watson A A 2000 *Rev. Mod. Phys.* **72** 689
[3] Knapp J 1997 *FZKA Report Forschungszentrum Karlsruhe* 5970
[4] Teshima M *et al* 1993 *Proc. 23rd Int. Cosmic Ray Conf. (Calgary)* Invited, Rapporteur, and Highlight Papers, ed D A Leahy *et al* (Singapore: World Scientific) p 257
[5] Greisen K 1966 *Phys. Rev. Lett.* **16** 748
[6] Zatsepin G T and Kuz'min V A 1966 *Zh. Eksp. Teor. Fiz., Pisma Red.* **4** 144
Zatsepin G T and Kuz'min V A 1966 *Sov. Phys. JETP Lett.* **4** 78
[7] Takeda M *et al*—AGASA Collaboration 1998 *Phys. Rev. Lett.* **81** 1163
[8] Bird D J *et al* 1995 *Astrophys. J.* **441** 144
[9] Jui Ch C H *Proc. 26th Int. Cosmic Ray Conf. (Salt Lake City)* Invited, Rapporteur, and Highlight Papers (AIP Conference Proceedings) vol 516, ed B L Dingus *et al*, p 370
[10] Knapp J *et al* 2003 *Astropart. Phys.* **19** 77
[11] Antoni T *et al*—KASCADE Collaboration 2003 *Nucl. Instrum. Methods* A at press
Klages H O *et al* 1997 *Nucl. Phys.* B *(Proc. Suppl.)* **52** 92
[12] Pierre Auger Project Design Report 1997, Pierre Auger Collaboration, Fermi National Accelerator Lab. www.auger.org/admin
Dova M T *et al*—Pierre Auger Observatory Collaboration 2001 *Proc. 27th Int. Cosmic Ray Conf. (Hamburg)* vol 2, p 699
[13] Auger P, Maze R and Grivet-Mayer T 1938 *C.R. Acad. Sci. Ser.* 2 **206** 172
Auger P, Maze R and Grivet-Mayer T 1938 *C.R. Acad. Sci. Ser.* 2 **207** 228
[14] Kohlhörster W, Matthes I and Webber E 1938 *Naturwissenschaften* **26** 576
[15] Heck D *et al* 1998 *FZKA Report Forschungszentrum Karlsruhe* 6019
[16] Gaisser T K and Hillas A M 1977 *Proc. 15th Int. Cosmic Ray Conf. (Plovdiv)* vol 8, p 353
[17] Jelley J V *et al* 1965 *Nature* **205** 327
[18] Askaryan G A 1962 *Sov. Phys. JETP* **14** 441

[19] Bernlöhr K 2002 Private communication
[20] Glasmacher M *et al* 1999 *Astropart. Phys.* **10** 291
[21] Borione A *et al* 2000 *Nucl. Instrum. Methods* A **346** 682
[22] Fowler J W *et al* 2001 *Astropart. Phys.* **15** 49
[23] Swordy S and Kieda D 2000 *Astropart. Phys.* **13** 137
[24] Arqueros F *et al* 2000 *Astron. Astrophys.* **359** 682
[25] Karle A *et al* 1995 *Astropart. Phys.* **3** 321
[26] Bernlöhr K *et al* 1999 *Astropart. Phys.* **5** 139
[27] Vernov S N 1979 *Proc. 16th Int. Cosmic Ray Conf. (Kyoto)* vol 8, p 129
[28] Fomin Y A *et al* 1991 *Proc. 22th Int. Cosmic Ray Conf. (Dublin)* vol 2, p 85
[29] Aglietta M *et al* 1989 *Nucl. Instrum. Methods* A **277** 23
[30] Ahlen M *et al* 1993 *Nucl. Instrum. Methods* A **324** 337
[31] Nagano M *et al* 1984 *J. Phys. G: Nucl. Part. Phys.* **10** 1295
[32] Teshima M *et al* 1992 *Nucl. Instrum. Methods* A **311** 338
[33] Doll P *et al* 2002 *Nucl. Instrum. Methods* A **488** 517
[34] Engler H *et al* 1999 *Nucl. Instrum. Methods* A **427** 528
[35] Bozdog H *et al* 2001 *Nucl. Instrum. Methods* A **465** 455
[36] Bertaina M *et al* 2001 *Proc. 27th Int. Cosmic Ray Conf. (Hamburg)* vol 2, p 792
[37] Chilingaryan A A *et al* 1999 *Proc. 24th Int. Cosmic Ray Conf. (Salt Lake City)* vol 1, p 240
[38] Daryan A V *et al* 2001 *Proc. 27th Int. Cosmic Ray Conf. (Hamburg)* vol 1, p 273
[39] Amenomori M *et al* 1996 *Astrophys. J.* **461** 408
[40] Bacci C *et al* 1999 *Proc. 26th Int. Cosmic Ray Conf. (Salt Lake City)* vol 5, p 265
[41] Lawrence M A *et al* 1991 *J. Phys. G: Nucl. Part. Phys.* **17** 773
[42] Agnetta G *et al* 1995 *Nucl. Instrum. Methods* A **359** 596
[43] Afanasiev N N *et al* 1995 *Proc. 24th Int. Cosmic Ray Conf. (Rome)* vol 2, p 756
[44] Cassidy G L *et al* 1985 *Rev. Nucl. Part. Sci.* **35** 351
[45] Bird D J *et al* 1993 *Phys. Rev. Lett.* **71** 3401
[46] Ito N *et al* 1997 *Proc. 25th Int. Cosmic Ray Conf. (Durban)* vol 4, p 117
[47] Hayashi Y *et al* 2001 *Proc. 27th Int. Cosmic Ray Conf. (Hamburg)* vol 1, p 111
[48] Dickinson J E *et al* 1997 *Proc. 26th Int. Cosmic Ray Conf. (Salt Lake City)* vol 3, p 136
[49] Antonov R A *et al* 2001 *Proc. 27th Int. Cosmic Ray Conf. (Hamburg)* vol 2, p 828
[50] Adriani O *et al* 2002 *Nucl. Instrum. Methods* A **488** 209
[51] Gress O A *et al* 1999 *Nucl. Phys.* B *(Proc. Suppl.)* **75** 299
[52] Alexejev E N *et al* 1979 *Proc. 16th Int. Cosmic Ray Conf. (Kyoto)* vol 10, p 276
[53] Bakatanov V N *et al* 1979 *Astropart. Phys.* **8** 59
[54] Shirasaki Y *et al* 2001 *Astropart. Phys.* **15** 357
[55] Baradzei L T *et al* 1992 *Nucl. Phys.* B **370** 365
[56] Akashi M *et al* 1981 *Phys. Rev.* D **24** 2353
[57] Ren J R *et al* 1981 *Phys. Rev.* D **38** 1414
[58] Kamata K and Nishimura J 1958 *Prog. Theoret. Phys. Suppl.* **6** 93
[59] Greisen K 1956 *Progress in Cosmic Ray Physics* vol 3 (Amsterdam: North-Holland)
[60] Greisen K 1960 *Ann. Rev. Nucl. Sci.* **10** 63
[61] Koneko T *et al* 1975 *Proc. 14th Int. Cosmic Ray Conf. (Munich)* vol 8, p 2747
[62] Coy R N *et al* 1997 *Astropart. Phys.* **6** 263
[63] Ave M *et al* 2001 *Proc. 27th Int. Cosmic Ray Conf. (Hamburg)* vol 1, p 385
[64] Vernov S N *et al* 1960 *Proc. 9th Int. Cosmic Ray Conf. (Moscow)* vol 2, p 7
[65] Aguirre C *et al* 1979 *J. Phys. G: Nucl. Part. Phys.* **5** 139
[66] Glasstetter R *et al*—KASCADE Collaboration 1999 *26th Int. Cosmic Ray Conf. (Salt Lake City)* vol 1, p 222
[67] Aglietta M *et al* 1999 *Astropart. Phys.* **10** 1
[68] Chilingarian A 1999 *26th Int. Cosmic Ray Conf. (Salt Lake City)* vol 1, p 240
[69] Honda K *et al* 2001 *Proc. 27th Int. Cosmic Ray Conf. (Hamburg)* vol 1, p 141
[70] Nesterova N M *et al* 1995 *Proc. 24th Int. Cosmic Ray Conf. (Rome)* vol 2, p 748
[71] Erlykin A D and Wolfendale A W 1999 *Astropart. Phys.* **10** 69
[72] Schatz G *et al* 2002 *Astropart. Phys.* **17** 13
[73] Hillas A M *et al* 1970 *Proc. 11th Int. Cosmic Ray Conf. (Budapest)* vol 3, p 533
[74] Khristiansen G B *et al* 1977 *Proc. 15th Int. Cosmic Ray Conf. (Plovdiv)* vol 8, p 148
[75] Stamenov J N *et al* 1979 *Trudy Fian SSSR* **109** 132
[76] Antoni T *et al*—KASCADE Collaboration 2001 *Astropart. Phys.* **14** 245

[77] Wdowczyk J 1994 *J. Phys. G: Nucl. Part. Phys.* **20** 1001
[78] Glasmacher M *et al* 1999 *Astropart. Phys.* **12** 1
[79] Watson A A and Wilson J G 1974 *J. Phys. A: Math. Gen.* **7** 1199
[80] Brancus I M *et al* 2003 *J. Phys. G: Nucl. Part. Phys.* **29** 453
[81] Hillas A M *et al* 1971 *12th Int. Cosmic Ray Conf. (Hobart)* vol 3, p 1001
Hillas A M 1981 *17th Int. Cosmic Ray Conf. (Paris)* vol 8, p 1993
[82] Kasahara S M *et al* 1997 *Phys. Rev.* D **55** 5282
[83] Petrera S 1996 *Nuovo Cimento* C **19** 737
[84] Aglietta M 1994 *Phys. Lett.* B **337** 376
[85] Haungs A *et al* 1996 *Nucl. Instrum. Methods* A **372** 515
[86] Freudenreich H *et al* 1990 *Phys. Rev.* D **41** 2732
[87] Aguirre C *et al* 2000 *Phys. Rev.* D **62** 032003
[88] Hörandel J R *et al*—KASCADE Collaboration 1999 *26th Int. Cosmic Ray Conf. (Salt Lake City)* vol 1, p 337
[89] Antoni T *et al*—KASCADE Collaboration 1999 *J. Phys. G: Nucl. Part. Phys.* **25** 2161
[90] Antoni T *et al*—KASCADE Collaboration 2001 *J. Phys. G: Nucl. Part. Phys.* **27** 1785
[91] Antoni T *et al*—KASCADE Collaboration 2003 Preparation of enriched cosmic ray mass groups with KASCADE *Astropart. Phys.* at press
[92] Slavatinski S A 1997 Private communication
[93] Haungs A and Kempa J 2001 *Proc. 27th Int. Cosmic Ray Conf. (Hamburg)* vol 1, p 22
[94] Augusto C R A *et al* 2000 *Phys. Rev.* D **61** 012003
[95] Huang J *et al* 2003 *Astropart. Phys.* **18** 637
[96] Kawasumi N *et al* 1996 *Nuovo Cimento* C **19** 1023
[97] Aguirre C *et al* 2000 *ICRR-Report* 4070-2000-14 *Tokio* 32
[98] Lindner A *et al* 1998 *Astropart. Phys.* **8** 235
[99] Cortina J *et al* 1997 *J. Phys. G: Nucl. Part. Phys.* **23** 1733
[100] Baltrusaitis R M *et al* 1985 *Nucl. Instrum. Methods* A **240** 410
[101] Matthews J N *et al*—HiRes Collaboration 2001 *Proc. 27th Int. Cosmic Ray Conf. (Hamburg)* vol 2, p 350
[102] Forschungszentrum Karlsruhe *Press Information* 2001/PI212001; http://www.fzk.de
[103] Nagano M *et al* 2001 *Proc. 27th Int. Cosmic Ray Conf. (Hamburg)* vol 1, p 424
[104] Allan H R 1971 *Progr. Elem. Part. Cosmic Ray Phys.* vol 10, ed J G Wilson and Wouthuysen (Amsterdam: North-Holland) p 171
[105] Falcke H and Gorham P 2002 *Astropart. Phys., Preprint* astro-ph/0207226, at press
[106] Scuitto S J 1999 *Preprint* astro-ph/9911331
[107] Stanev T 1999 *Proc. 26th Int. Cosmic Ray Conf. (Salt Lake City)* Invited, Rapporteur, and Highlight Papers (AIP Conference Proceedings) vol 516, ed B L Dingus *et al*, p 247
[108] Engel R 2001 *Proc. 27th Int. Cosmic Ray Conf. (Hamburg)* Invited, Rapporteur, and Highlight Papers, ed R Schlickeiser, p 181
[109] Chilingarian A A 1989 *Comput. Phys.* **54** 381
Chilingarian A A *et al* 1997 *Nucl. Phys.* B *(Proc. Suppl.)* **52** 237
[110] Weber J *et al*—KASCADE Collaboration 1999 *26th Int. Cosmic Ray Conf. (Salt Lake City)* vol 1, p 341
[111] Röhring A *et al* 1999 *Proc. 26th Int. Cosmic Ray Conf. (Salt Lake City)* vol 3, p 152
[112] Röhring A *et al* 1999 *Proc. 26th Int. Cosmic Ray Conf. (Salt Lake City)* vol 1, p 214
[113] Fox L and Goodwin E T 1953 *Phil. Trans. R. Soc. Ser.* A **245** 501
[114] Blobel V 1984 *CERN School of Computing, Published by CERN (Aiguablava) 1985*
[115] D'Agostini G 1995 *Nucl. Instrum. Methods* A **362** 487
[116] Gold R 1964 *Argonne National Laboratory Report* ANL-6984
[117] Roth M *et al*—KASCADE Collaboration 2002 *Proc. 12th ISVHECRI, CERN, Nucl. Phys.* B *(Proc. Suppl.)* at press
[118] Bishop C M 1995 *Neural Networks for Pattern Recognition* (Oxford: Oxford University Press)
[119] Fukunaka K 1972 *Introduction to Statistical Pattern Recognition* (New York: Academic)
[120] Bayes T 1763 *Phil. Trans. R. Soc.* **53** 54 (reprinted in 1958 *Biometrika* **45** 296)
[121] Parzen E 1962 *Ann. Math. Stat.* **33** 1065
[122] Antoni T *et al*—KASCADE Collaboration 2002 *Astropart. Phys.* **16** 245
[123] Peters B 1991 *Nuovo Cimento* **22** 800
[124] Drury L O C 1983 *Rep. Prog. Phys.* **46** 973
[125] Kirk J G and Dendy R O 2001 *J. Phys. G: Nucl. Part. Phys.* **27** 1589
[126] Berezhko E G and Ksenofotov L T 1999 *Sov. Phys. JETP* **89** 397
[127] Biermann P L 1993 *Astron. Astrophys.* **271** 649

[128] Cesarsky C J 1980 *Ann. Rev. Astron. Astrophys.* **18** 289
[129] Gaisser T K 2000 *Proc. High-Energy Gamma-Ray Astr. (Heidelberg)* (AIP Conf. Proc.) vol 558, p 27
[130] Ptuskin V S *et al* 1997 *Astron. Astrophys.* **321** 434
[131] Erlykin A D and Wolfendale A W 1997 *J. Phys. G: Nucl. Part. Phys.* **23** 979
[132] Nikolsky S I 1995 *Nucl. Phys. Proc. Suppl.* A **39** 157
[133] Nikolsky S I and Romachin R 2000 *Phys. Atomic Nucl.* **63** 1799
[134] Wigmans R 2003 *Astropart. Phys.* **19** 379
[135] Kazanas D and Nicolaidis A 2001 *Astropart. Phys., Preprint* hep-ph/0109247
[136] Haungs A 2003 *J. Phys. G: Nucl. Part. Phys.* **29** 809
[137] Knurenko S *et al* 2001 *Proc. 27th Int. Cosmic Ray Conf. (Hamburg)* vol 1, p 145
[138] Ulrich H *et al*—KASCADE Collaboration 2001 *Proc. 27th Int. Cosmic Ray Conf. (Hamburg)* vol 1, p 97
[139] Navarra G *et al* 2001 *Proc. 27th Int. Cosmic Ray Conf. (Hamburg)* vol 1, p 120
[140] Prosin V V *et al* 2002 Private communication
[141] Paling S *et al* 1997 *Proc. 25th Int. Cosmic Ray Conf. (Durban)* vol 5, p 253
[142] Boothby *et al* 1997 *Astrophys. J.* **491** L35
[143] Hörandel J *et al*—KASCADE Collaboration 2001 *Proc. 27th Int. Cosmic Ray Conf. (Hamburg)* vol 1, p 137
[144] Rebel H *et al* 1995 *J. Phys. G: Nucl. Part. Phys.* **21** 451
[145] Büttner C *et al*—KASCADE Collaboration 2001 *Proc. 27th Int. Cosmic Ray Conf. (Hamburg)* vol 1, p 153
[146] Engler J *et al*—KASCADE Collaboration 1999 *26th Int. Cosmic Ray Conf. (Salt Lake City)* vol 1, p 349
[147] Antoni T *et al*—KASCADE Collaboration 2002 *Astropart. Phys.* **16** 373
[148] Allesandro B—EAS-TOP Collaboration *et al* 2001 *Proc. 27th Int. Cosmic Ray Conf. (Hamburg)* vol 1, p 127
[149] Kampert K-H *et al*—KASCADE Collaboration 2002 *Proc. 27th Int. Cosmic Ray Conf. (Hamburg)* Invited, Rapporteur, and Highlight Papers, ed R Schlickeiser, p 240
[150] Ulrich H *et al*—KASCADE Collaboration 2002 *Proc. 12th ISVHECRI, CERN*, *Nucl. Phys.* B *(Proc. Suppl.)* submitted
[151] Roth M *et al*—KASCADE Collaboration 2001 *Proc. 27th Int. Cosmic Ray Conf. (Hamburg)* vol 1, p 88
[152] Kalmykov N N and Khristiansen G B 1995 *J. Phys. G: Nucl. Part. Phys.* **21** 1279
[153] Stanev T *et al* 2000 *Phys. Rev.* D **62** 093005
[154] Tinyakov P and Tkachev I 2002 *Talk given at International Workshop on Extremely High Energy Cosmic Rays (Wako, Japan, 5–6 November 2002) Preprint* hep-ph/0212223
[155] Evans N W, Ferrer F and Sarkar S 2002 *Preprint* hep-ph/0212533
[156] Linsley J 1963 *Phys. Rev. Lett.* **10** 146
[157] Winn M M *et al* 1986 *J. Phys. G: Nucl. Part. Phys.* **12** 653
[158] Ave M *et al* 2003 *Astropart. Phys.* **19** 47
[159] Efimov N N *et al* 1991 *Proc. Int. Symp. Astrophysical Aspects of the Most Energetic Cosmic Rays* ed M Nagano and F Takahara, p 20
[160] Yoshida S *et al* 1995 *Astropart. Phys.* **3** 105
[161] Sakaki N *et al* 2001 *Proc. 27th Int. Cosmic Ray Conf. (Hamburg)* vol 1, p 333
[162] Abu-Zayyad T *et al* 2003 *Phys. Rev. Lett., Preprint* astro-ph/0208243 at press
[163] Abu-Zayyad T *et al* 2003 *Astropart. Phys., Preprint* astro-ph/0208301, at press
[164] Sommers P 2002 *Proc. 27th Int. Cosmic Ray Conf. (Hamburg)* Invited, Rapporteur, and Highlight Papers, p 170
[165] Ave M *et al* 2003 *Astropart. Phys.* **19** 61
[166] Glushov A V *et al* 2002 *Phys. At. Nucl.* **65** 1313
[167] Antonov E E *et al* 1999 *Sov. Phys. JETP Lett.* **69** 650
[168] Abu-Zayyad T *et al* 2001 *Astrophys. J.* **557** 686
[169] Watson A A 1991 *Nucl. Phys.* B *(Proc. Suppl.)* **22** 116
[170] Bahcall J N and Waxman E 2002 *Preprint* hep-ph/0206217
[171] Takeda M *et al* 1998 *Phys. Rev. Lett.* **81** 1163
[172] Takeda M *et al* 1999 *Astrophys. J.* **522** 225
[173] Takeda M *et al* 2003 *Astropart. Phys.* **19** 447
[174] Teshima M 2002 Private communication
[175] Berezinsky V, Gazizov A Z and Grigorieva S I *Preprint* hep-ph/0204357
[176] Pravdin M I *et al* 1999 *Proc. 26th Int. Cosmic Ray Conf. (Salt Lake City)* vol 3, p 292
[177] Heck D 2002 Private communication
[178] Abu-Zayyad T *et al* 2000 *Phys. Rev. Lett.* **84** 4276
[179] Dyakonov M N *et al* 1993 *Proc. 23th Int. Cosmic Ray Conf. (Calgary)* vol 4, p 303
[180] Drescher H-J *et al* 2001 *Phys. Rep.* **350** 93

[181] Gaisser T K *et al* 1993 *Phys. Rev.* D **47** 1919
[182] Hayashida N *et al* 1995 *J. Phys. G: Nucl. Part. Phys.* **21** 1101
[183] Dawson B R *et al* 1998 *Astropart. Phys.* **9** 331
[184] Ave M *et al* 2000 *Phys. Rev. Lett.* **85** 2244
Ave M *et al* 2001 *Proc. 27th Int. Cosmic Ray Conf. (Hamburg)* vol 1, p 390
[185] Shinozaki K *et al* 2002 *Astrophys. J.* **571** L117
[186] Hayashida N *et al* 1999 *Astropart. Phys.* **10** 303
[187] Dai H *et al* 1999 *Astrophys. J.* **511** 739
[188] Gribov V N 1968 *Sov. Phys. JETP* **26** 414
[189] Fetcher R S *et al* 1994 *Phys. Rev.* D **50** 5710
[190] Engel R 1999 *26th Int. Cosmic Ray Conf. (Salt Lake City)* vol 1, p 415
[191] Kalmykov N N *et al* 1997 *Nucl. Phys.* B *(Proc. Suppl.)* **52** 17
[192] Werner K 1993 *Phys. Rep.* **232** 87
[193] Ranft J 1995 *Phys. Rev.* D **51** 64
[194] Jones L 2002 *CERN COURIER* vol 42, No 6 (July/August 2002) p 26
[195] See talks at the NEEDS-workshop's webpage: http://www-ik.fzk.de/~needs
[196] Engel R 2002 *Proc. 12th ISVHECRI, CERN, Nucl. Phys.* B *(Proc. Suppl.), Preprint* astro-ph/0212340, at press
[197] Schatz G 2002 *Proc. 12th ISVHECRI, CERN, Nucl. Phys.* B *(Proc. Suppl.)* at press
[198] Hara T *et al* 1983 *Phys. Rev. Lett.* **50** 2058
[199] Baltrusaites R M *et al* 1984 *Phys. Rev. Lett.* **52** 1380
[200] Honda *et al* 1993 *Phys. Rev. Lett.* **70** 525
[201] Maier G *et al*—KASCADE Collaboration 2001 *Proc. 27th Int. Cosmic Ray Conf. (Hamburg)* vol 1, p 161
[202] Chilingarian A A *et al* 2001 *Proc. 27th Int. Cosmic Ray Conf. (Hamburg)* vol 1, p 165
[203] Alvarez-Muñiz J *et al* 2002 *Phys. Rev.* D **66** 123004
[204] Saavedra O 2001 Nuclei far from stability and astrophysics *NATO Science Series II* vol 17, ed D N Poenaru *et al* (Dordrecht: Kluwer) p 385
[205] Völk H J and Biermann P L 1988 *Astrophys. J.* **333** L65
[206] Biermann P L, Gaisser T K and Stanev T 1995 *Phys. Rev.* D **51** 3450
[207] Pelletier G 2001 *Lecture Notes in Physics vol 576* ed M Lemoine and G Sigl (Berlin: Springer) p 58
[208] Swordy S 1995 *Proc. 24th Int. Cosmic Ray Conf. (Rome)* vol 2, p 697
[209] Waxman E W 1995 *Phys. Rev. Lett.* **75** 386
[210] Hillas A M 1984 *Ann. Rev. Astron. Astrophys.* **22** 425
[211] Stecker F W 2002 *Proc. 7th Paris Cosmology Colloquium on High Energy Astrophysics for and from Space* ed H J de Vega and N G Sanchez *Preprint* astro-ph/0207629
[212] Ahn E-J *et al* 1999 *Preprint* astro-ph/9911123
[213] Stecker F W and Salamon M H 1999 *Astrophys. J.* **512** 521
[214] Bhattarcharjee P and Sigl G 2000 *Phys. Rep.* **327** 109
[215] Fodor Z *et al* 2002 *Phys. Rev. Lett.* **88** 171101
[216] Domokos G and Kovesi-Domokos S 1988 *Phys. Rev.* D **38** 2933
[217] Sato H and Tati T 1972 *Prog. Theor. Phys.* **47** 1788
[218] Dubovsky S L and Tinyakov P G 2002 *Astropart. Phys.* **18** 89
[219] Aloisio R *et al* 2000 *Phys. Rev.* D **62** 053010
[220] Aharonian F *et al* 1992 *Phys. Rev.* D **46** 4188
[221] Halzen F 2003 *Proc. XXI Symp. Relativistic Astroph. (Florence, Italy)* at press, *Preprint* astro-ph/0302489
[222] Kieda D B, Swordy SP and Wakely S P 2001 *Astropart. Phys.* **15** 287
[223] Wefel J P 2003 *J. Phys. G: Nucl. Part. Phys.* **29** 821
[224] Clem J *et al* 2002 *Astropart. Phys.* **16** 387
[225] Khrenov B A *et al* 2002 *Nucl. Phys.* B *(Proc. Suppl.)* **113** 115
[226] Yoshida S and Dai H 1998 *J. Phys. G: Nucl. Part. Phys.* **24** 905
[227] Ulrich R 2002 *FZKA Report Forschungszentrum Karlsruhe* 6787
[228] Ostapchenko S 2003 *J. Phys. G: Nucl. Part. Phys.* **29** 831
[229] Aiso S *et al* 1997 *Proc. 25th Int. Cosmic Ray Conf. (Durban)* vol 5, p 373
[230] Mathes H-J 2002 Private communication
[231] Scarsi L *et al* OWL/AIRWATCH Collaboration 2001 *Proc. 27th Int. Cosmic Ray Conf. (Hamburg)* vol 2, p 384
[232] Scarsi L *et al*—EUSO Team 2001 *Proc. 27th Int. Cosmic Ray Conf. (Hamburg)* vol 2, p 839
[233] Gaisser T K, Halzen F and Stanev T 1995 *Phys. Rep.* **258** 173
[234] Medina Tanco G A 1998 *Astrophys. J.* **505** L79